Coastal monitoring solutions of the geomorphological response of beach-dune systems using multi-temporal LiDAR datasets (Vendée coast, France)

Article *in* Geomorphology · March 2018

DOI: 10.1016/j.geomorph.2017.12.037

CITATIONS
16

READS
522

6 authors, including:

Martin Juigner
University of Nantes
13 PUBLICATIONS **42** CITATIONS

SEE PROFILE

Antoine Ba
Airbus Defence and Space
12 PUBLICATIONS **37** CITATIONS

SEE PROFILE

Marc Robin
University of Nantes
141 PUBLICATIONS **573** CITATIONS

SEE PROFILE

Geomorphology 304 (2018) 121–140

Contents lists available at ScienceDirect

Geomorphology

journal homepage: www.elsevier.com/locate/geomorph

Coastal monitoring solutions of the geomorphological response of beach-dune systems using multi-temporal LiDAR datasets (Vendée coast, France)

Baptiste Le Mauff [a,*], Martin Juigner [a], Antoine Ba [b], Marc Robin [a], Patrick Launeau [b], Paul Fattal [a]

[a] Littoral Environnement Télédétection Géomatique, UMR 6554 CNRS, Université de Nantes, Campus Tretre, BP 81227, 44312 Nantes Cedex 3, France
[b] Laboratoire de Planétologie & Géodynamique, UMR 6112 CNRS, Université de Nantes, 2 Rue de la Houssinière, BP 92208, 44322 Nantes Cedex 3, France

ARTICLE INFO

Article history:
Received 24 May 2017
Received in revised form 20 December 2017
Accepted 26 December 2017
Available online 5 January 2018

Keywords:
Coastal monitoring
DEM of Difference (DoD)
Sediment budget
Shoreline erosion and accretion

ABSTRACT

Three beach and dune systems located in the northeastern part of the Bay of Biscay in France were monitored over 5 years with a time series of three airborne LiDAR datasets. The three study sites illustrate a variety of morphological beach types found in this region. Reproducible monitoring solutions adapted to basic and complex beach and dune morphologies using LiDAR time series were investigated over two periods bounded by the three surveys. The first period (between May 2008 and August 2010) is characterized by a higher prevalence of storm events, and thus has a greater potential for eroding the coast, than the second period (between August 2010 and September 2013). During the first period, the central and northeastern part of the Bay of Biscay was notably impacted by Storm Xynthia, with water levels and wave heights exceeding the 10-year return period and 1-year return period, respectively. Despite differences in dune morphology between the sites, the dune crest (D_{high}) and the dune base (D_{low}) are efficiently extracted from each DEM. Based on the extracted dune base, an original shoreline mobility indicator is built displaying a combination of the horizontal and vertical migrations of this geomorphic indicator between two LiDAR datasets. A 'Geomorphic Change Detection' is also completed by computing DEMs of Difference (DoD) resulting in segregated maps of erosion and deposition and sediment budgets. Accounting for the accuracy of LiDAR datasets, a probabilistic approach at a 95% confidence interval is used as a threshold for the Geomorphic Change Detection showing more reliable results. However, caution should be taken when interpreting thresholded maps of changes and sediment budgets because some beach processes may be masked, especially on wide tidal beaches, by only keeping the most significant changes. The results of the shoreline mobility and Geomorphic Change Detection show a high variability in the beach responses between and within the three study sites, explained mainly by beach orientation and local factors. Despite variable site-specific mechanisms, the recovery processes redistribute the available sand more on the upper parts of the beach, producing significant deposition generally in the form of embryo dunes. The monitoring of the beach and dune systems with airborne LiDAR datasets reveals that the three study sites show diverse behaviours during the first period likely associated with storms, while the analysis show more homogenous beach responses during the second period likely associated with a recovery phase.

1. Introduction

The geomorphological resilience of a system is determined by the degree to which it returns to an equilibrium state following a disturbance (Brunsden, 2001; Woodroffe, 2007; Houser et al., 2015). In a coastal system, significant morphological changes occur during severe storms or a succession of storm events (Lee et al., 1998), combined with high water levels (Short, 1991; Zhang et al., 2001; Cooper et al., 2004). Depending on the magnitude, duration and succession of such events, the coastal system can return to a transient or a new equilibrium state different from the pre-disturbance state (Cowell and Thom, 1995; Woodroffe, 2007; Houser and Hamilton, 2009; Scott et al., 2016). Moreover, such events impact the coastal system over hours to days, while the recovery of the beach can take days, months (Wang et al., 2006; Pye and Blott, 2008) or up to several years or decades for a full recovery of the system (Thom and Hall, 1991; Lee et al., 1998; Suanez et al., 2012; Houser et al., 2015; Castelle et al., 2017). The recovery of a beach system comprises complex processes as many morphological responses are apparent in field observations and measurements (Houser and Hamilton, 2009; Priestas and Fagherazzi, 2010; Scott et al., 2016; Castelle et al., 2017).

Repeated topographic surveys are necessary to monitor morphological changes in beaches (Thom and Hall, 1991). Topographic measurements are traditionally performed with ground-based techniques such as dGPS or total stations. Without equipped manpower or adapted vehicles, they are cost- and time-effective only on small and accessible

* Corresponding author.
E-mail address: baptiste.le-mauff@univ-nantes.fr (B. Le Mauff).

https://doi.org/10.1016/j.geomorph.2017.12.037
0169-555X/

beaches (Baptista et al., 2008). Since the 1970s, LiDAR technology has been developed (Krabill et al., 2000; Brock and Purkis, 2009). In coastal studies, airborne LiDAR associated with kinematic GPS provides rapid, accurate, continuous, and high-resolution topographic datasets over large areas (Krabill et al., 2000; Sallenger Jr. et al., 2003). Compared to beach profile surveys that provide discrete data sampling in two dimensions, airborne LiDAR surveys provide more convenient and synoptic topographic data of the beach in three dimensions (Woolard and Colby, 2002; Zhang et al., 2005; Pye and Blott, 2016) from which many morphometric parameters can be derived (Brock et al., 2004; Saye et al., 2005).

Structure from motion (SfM) techniques are a good alternative to time-consuming ground-based measurements and costly LiDAR campaign. Recent development of camera-equipped unmanned aerial vehicles (UAVs) provides high resolution topographic datasets suitable for observing morphological change in beaches (Mancini et al., 2013). They are a cheap and convenient powerful tool for geomorphic change detection (Cook, 2017), but they are generally deployed on smaller spatial extent than airborne LiDAR campaign. However, topographic measurements such as LiDAR surveys are only "snapshots" of a beach state (Woolard and Colby, 2002; Pye and Blott, 2016), and as beaches are not surveyed immediately before and after each event, the changes observed should be interpreted with caution. A newly developed method using radar technology offers a tool for quantifying morphological changes over large areas and at high temporal resolution (Bell et al., 2016; Bird et al., 2017). Even if the vertical accuracy of the elevation maps produced with this method doesn't reach the one of LiDAR-derived DEMs, this technique appears sufficient and efficient to monitor seasonal change of bedforms as well as storm impact on intertidal areas.

The post-processing of LiDAR point clouds produces high quality DEMs (Woolard and Colby, 2002; White and Wang, 2003; Liu and Zhang, 2008). When a time series of LiDAR data is available, a volumetric change analysis can be performed by subtracting two DEMs on a cell-by-cell basis to create a *DEM of Difference* (DoD) (Wheaton et al., 2010) or *Elevation Change Map* (ECM) (Priestas and Fagherazzi, 2010). The DoD provides a map of erosion and deposition from which sediment budgets can be computed (Zhang et al., 2005; Thornton et al., 2006; Wheaton et al., 2010). The simple difference between two topographic datasets is a raw estimate of geomorphic change. A reliable quantification of geomorphic change must account for the uncertainty inherent in the data used to compute the DoD (Brasington et al., 2000; Wheaton et al., 2010). Moreover, a great deal of noise is inherent in airborne LiDAR measurements because of their high resolution (generally 1 to 5 m) and vertical accuracy (generally 10 to 20 cm) (Krabill et al., 2000; Sallenger Jr. et al., 2003). Usually, a detection threshold is estimated using the RMS difference with a survey with ground control points (Sallenger Jr. et al., 2003; Thornton et al., 2006) or the RMS difference between two surveys computed on hard surfaces like roads or parking lots (Zhang et al., 2005; Young and Ashford, 2006). Accounting for uncertainty to detect significant geomorphic changes from LiDAR using this methodology has not been discussed enough or explicitly in coastal studies. Another methodology to estimate a detection threshold based on a probabilistic approach has been used for almost twenty years for fluvial environments (Brasington et al., 2003; Wheaton et al., 2010) and only recently for a coastal environment (Autret et al., 2016).

Mapping the shoreline and its migration over time is one of the foremost methodologies used to investigate beach changes (Crowell et al., 1991). Traditionally obtained during field surveys or from digitizing aerial images, the delineation of a shoreline is based on the visual interpretation and perception of the analyst. The digitized feature's accuracy and shape can vary between analysts depending on their experience and knowledge, even if the same procedure is applied on the same dataset (Rutzinger et al., 2012; Ruggerio et al., 2013; Palaseanu-Lovejoy et al., 2016). The availability of LiDAR datasets enables a shoreline to be extracted more objectively, and potentially more rapidly, than the traditional time-consuming procedures over beaches several kilometers long (Stockdon et al., 2002; Woolard and Colby, 2002; Baptista et al., 2008; White et al., 2011; Ruggerio et al., 2013).

Depending on the objectives of the study, the shoreline is extracted from LiDAR-derived DEMs as a datum-based line such as the Mean High Water (MHW) level (Stockdon et al., 2002; Ruggiero et al., 2003; Moore et al., 2006; Robertson et al., 2007), or as a geomorphic feature like the dune base (D_{low}) or the foredune crest (D_{high}) (Elko et al., 2002; Houser et al., 2008; Stockdon et al., 2009; Suanez et al., 2012). Whereas extracting a datum-based line from a DEM is rather straightforward, extracting the dune base (D_{low}) or the foredune crest (D_{high}) is more challenging as their height and shape vary between and within different beach-dune systems. As LiDAR surveys usually cover large areas, developing a fully reproducible and comparable procedure to extract geomorphic features automatically in irregular shaped topography like a beach-dune system has become a key methodological issue. To our knowledge, three principal methodologies for this kind of almost automatic extraction are used on beach areas: the detection of the highest elevation peak landward of the shoreline (Stockdon et al., 2009), the Least Cost Path extraction (Mitasova et al., 2011; Hardin et al., 2012), and an extraction based on the second derivative (curvature) of the elevation data (Gao, 2009; Hugenholtz and Barchyn, 2010; Hugenholtz et al., 2012; Rutzinger et al., 2012). Stockdon et al. (2009) developed a profile-based approach to extract the dune crest (D_{high}) where the foredune is the top of the dune field. The Least Cost Path approach (Mitasova et al., 2011; Hardin et al., 2012) preserves the resolution of the input DEM because it is based on a cell-by-cell basis, but it is also adapted to dune systems where the foredune reaches the highest elevation. However, these two methodologies may not be applicable to every dune system because the crest of the foredune is not always the top of the dune field, e.g. some sections of our study sites are characterized by multiple dune ridges. The curvature-based approach can differ between studies using, for example, filtering windows or thresholds that can be adapted to the study site morphology or study purposes. Yet, this generally requires the generation of cross-shore beach profiles from the DEM on which the analysis is performed. Unlike the Least Cost Path methodology, the delineation of the beach features has an alongshore resolution corresponding to the user-defined transect spacing, which is usually coarser than the initial DEM resolution.

Regardless of the methodology used to delineate a shoreline, the horizontal movement of the chosen shoreline serves as a binary indicator of the beach state: seaward (positive) displacement indicates accretion, whereas landward (negative) displacement indicates erosion (Dolan et al., 1991; Moore, 2000; Boak and Turner, 2005). Furthermore, the vertical movement, i.e. the height variation, of a geomorphic feature like the dune base (D_{low}) or the dune crest (D_{high}) is also a good indicator of the evolution of beach vulnerability (Houser et al., 2008; Stockdon et al., 2009; Suanez et al., 2012). However, located between the foredune and the beach, the dune base (D_{low}) is a good indicator of the coastal processes operating on any particular beach (Hesp, 2002). Despite its importance, the migration of the dune base (D_{low}) in both horizontal and vertical directions has not received much attention (Crapoulet et al., 2017). According to one hypothesis, depending on the geomorphological setting of the beach, the response of the dune base (D_{low}) to an extreme event and its resilience is a combination of a horizontal and a vertical movement.

The aim of this paper is to propose reproducible monitoring solutions adapted to basic and complex beach and dune morphologies using LiDAR time series. LiDAR datasets enable to monitor beach responses to sequences of storms and fair-weather conditions. Two indicators commonly employed in the scientific literature are computed: the sediment budget and dune base (D_{low}) migration. Sediment budgets are obtained by implementing a 'Geomorphic Change Detection' methodology originating from fluvial environment studies (Wheaton et al., 2010) using a probabilistic detection threshold, instead of a traditional RMS error (Zhang et al., 2005), to distinguish significant changes from

raw (unthresholded) volume estimations, and to assess the benefits and limitations of this methodology in a beach environment.

The beach and the dune work as a complex system in which beach responses, processes and rates of recovery vary between each interconnected subsystem (Scott et al., 2016). The dune crest (D_{high}), the dune base (D_{low}) and the MHW level are used in this paper to isolate each selected subsystem, i.e. the back dune, the foredune, the upper beach, and the tidal beach. Geomorphic Change Detection is operated through this cross-shore segregation to assess the variable beach responses within the system. To execute these geomorphic extractions, the challenge is to develop a new method based on the curvature approach, which is efficiently reproducible along sandy coasts characterized by complex and variable dune morphology, i.e. from a simple foredune ridge to multiple dune ridges with blow-outs. Lastly, the monitoring of the geomorphological response of the beach and dune systems is completed by an original shoreline mobility indicator displaying a combination of the horizontal and vertical movements of the dune base between two LiDAR datasets.

Through this approach, three study sites in Northern Vendée (France) with different geomorphological settings are analyzed, totaling 11 km of beach length. Although the availability of LiDAR datasets influenced site selection, the study sites represent the variety of morphological beach types found in this region. The beach responses were monitored over 5 years with a time series of 3 LiDAR datasets. Within the dates of the three LiDAR measurements, two contrasting periods can be distinguished. The first two years, between May 2008 and August 2010, are characterized by a succession of several storms including Storm Xynthia in February 2010 whose storm surge reached the 100-year return period in several tide gauges of the central part of the Bay of Biscay (Pineau-Guillou et al., 2012). During the next three years, no major storm occurred until fall 2013, which is favorable for the recovery of the beach and dune system (Thom and Hall, 1991). Due to the low temporal resolution of the LiDAR surveys, the observed changes cannot be attributed to any particular storm event. Hence likely causes of the overall changes during the two periods considered can only be inferred.

2. Study sites

2.1. General geomorphological context

The study area is located in the North-East Atlantic Ocean, in the northeastern part of the Bay of Biscay, in the Vendée region of France between the Armorican massif and the Aquitanian coastal sedimentary basin. It is situated south of the Loire river incised-valley (Chaumillon et al., 2008) where the continental shelf can reach up to 200 km wide. The irregular shoreline is interrupted by a large embayment, Bourgneuf Bay, characterized by extensive intertidal mudflats bordered by one of the biggest marshes of the French Atlantic coast, i.e. the Marais Breton (450 km^2), as well as polders reclaimed up to the beginning of the 20th century (Verger, 2009). These coastal lowlands are located below high-tide levels and sometimes below the mean sea level. They are protected from ocean swell by the discontinuous dune ridges of Noirmoutier Island and the Pays-de-Monts forest (Fig. 1a).

The dune ridges of the study area developed during the Holocene (Morzadec-Kerfourn, 1995; Ters, 1961) at different orientations articulated around rocky outcrops or platforms (Fig. 1a). The southern end of Noirmoutier Island is formed by a sand spit oriented NW-SE. It is separated from the Pays-de-Monts dune ridge by the dynamic Fromentine inlet characterized by a large ebb-tidal delta (Fig. 1a). Yeu Island is located 20 km offshore of the Pays-de-Monts forest. The area bounded by Yeu Island, Noirmoutier Island, and Pays-de-Monts beaches is shallow and complex: the depth is <15 m NGF, and the bottom is characterized by large rocky platforms such as the Pont d'Yeu or the Boeufs platform (Fig. 1a).

Over the study area, the three selected study sites have different geomorphic configurations. They are presented in the following subsections from north to south.

2.2. Luzeronde

Luzeronde beach is located in the NW part of Noirmoutier Island (Fig. 1a). It is a 2 km-long embayed beach oriented NW between two rocky headlands (Herbaudière and Devin). The beach is backed by narrow dunes with a simple foredune ridge between 8 m and 12 m high (Figs. 1b, 5a). At low spring tide, rocky platforms may emerge from the shoreface on the southern part of the beach, which is more exposed to chronic coastal erosion. Several types of sea defenses have been built around Devin Point since the middle of the 19th century, such as sea-walls, ripraps, groins, and rows of wooden stakes used to dissipate wave energy. The northern part of the beach is more sheltered, with a chronic sand accumulation. Thus, the net alongshore drift is estimated at <10,000 m^3/year in a northward direction (DHI and GEOS, 2008).

2.3. Tresson

The second site is a rectilinear portion of Tresson beach located at the beginning of the southern sand spit of Noirmoutier Island (Fig. 1a), 3.5 km long and oriented SW. The beach is backed by large dunes with a simple foredune ridge between 8 m and 14 m high interrupted by noticeable blow-outs (Figs. 1c, 5b). The shoreface and the intertidal beach are flat and muddy. The northern part of the sand spit is characterized by a sediment deficit and cement or rock groins across the beach. The net alongshore drift is estimated to be oriented southward, reaching 25,000 m^3/year (DHI and GEOS, 2008). Within the studied portion of the sand spit, German casemates are today located on the upper beach at the bottom of the dunes they were built on. They are evidence of a constant dune retreat since World War II.

2.4. Pays-de-Monts

The third site is the northern part of Pays-de-Monts forest (Fig. 1a). The segment of beach is 6 km long, approximately rectilinear and oriented W. This wide dissipative beach lies between the Fromentine inlet and the Pont-d'Yeu rocky platform. The northern end of the studied portion is strongly influenced by the tidal inlet dynamics. Unfortunately, the emerged area covered by the ebb-tidal delta at low tide was not entirely surveyed. With the exception of the ebb-tidal delta characterized by ripples and megaripples and channel-shoal migration (Hayes, 1980; Verger, 2009; CREOCEAN, 2011), the tidal beach is wide and flat. It is backed by large dunes extended by Pays-de-Monts forest. The dune field has complex and multiple successive dune ridges, with the foredune being generally the lowest ridge (Figs. 1d, 5c). The foredune is between 6 m and 14 m high with an irregular shape as it can be interrupted by blow-outs. The net alongshore drift of this beach portion is estimated to be 20,000 m^3/year in a northward direction (DHI and GEOS, 2008). The only artificial beach segment of the northern part of Pays-de-Monts is located south between the studied portion and the Pont-d'Yeu rocky platform. This artificial shoreline is composed of sea walls and cement slipways overhung by a promenade.

3. Hydrodynamic setting

3.1. General hydrodynamic setting

Tides are semi-diurnal with a range reaching up to 6 m during spring tides (SHOM, 2014). According to the coast classification developed in Davies (1964), the coast can be considered macro-tidal.

A description of the wave climate is provided by Butel et al. (2002) based on buoy records. The Yeu buoy analyzed in their study is located 4 km west of the island at a depth of 33 m. It collected data from July

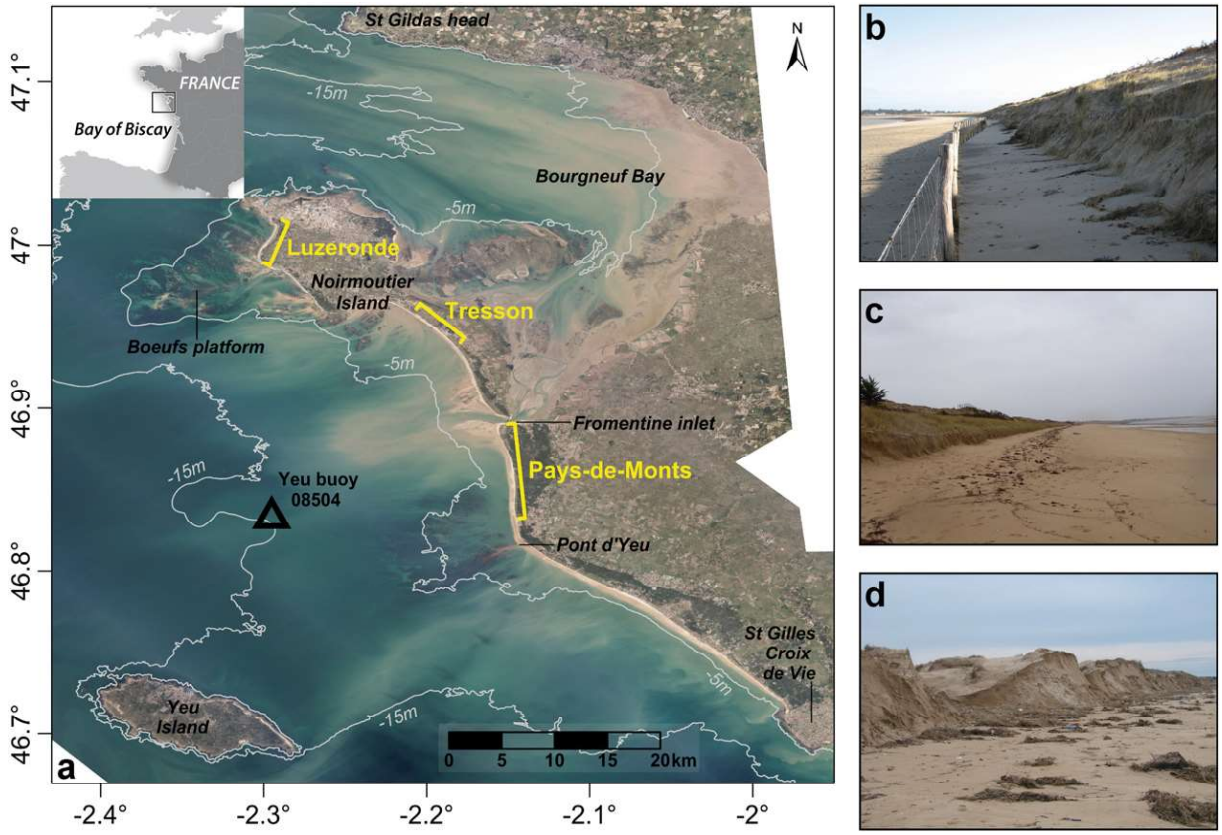

Fig. 1. (a) Location map of the three study sites between brackets and isobath lines (−5 m and −15 m NGF). Photographs of dune scarps and different dune morphologies showing the various impacts of Storm Xynthia at the sites of (b) Luzeronde (source: M. Paillart), (c) Tresson (source: M. Paillart), and (d) North Pays-de-Monts (source: *Observatoire du Littoral des Pays-de-Monts*).

1998 to January 2000. During this period, the mean annual significant wave height was 1.81 m, with a maximum of 8.88 m. The mean significant wave height was about 2.16 m in winter and 1.35 m in summer. The mean-annual mean period (T02) was 5.89 s with a maximum of 12.1 s; it ranged from 5 s to 7 s between summer and winter. The direction of the most frequent waves is from two main sectors, W-WNW and WSW-W, with larger waves coming from the WSW-W sector (Butel et al., 2002).

The wave climate variability in the Bay of Biscay was analyzed over a longer period (1953–2009) in a study report (CREOCEAN, 2011) with a model developed by Dodet et al. (2010) based on the WAVEWATCH III model (Tolman, 2009). The study report displays the results of the regional model extracted offshore of the study area at 50 m depth (CREOCEAN, 2011). They provide additional information about some parameters of the wave climate. In terms of significant wave height, winters are characterized by higher waves than the buoy observations (Butel et al., 2002), reaching >4 m. Wave height also shows a significant inter-annual variability, especially between winters: the significant wave height reaches 5 m during some winters and it doesn't exceed 3 m during others (CREOCEAN, 2011). The period is more variable between winters and summers than it is in the buoy observation: the point extraction in the model displays a peak period (Tp) ranging from 13 s in winter to 7 s in summer. Unlike significant wave height, peak period (Tp) shows less inter-annual variability.

The wave propagation from offshore to the study sites is strongly altered by the nearshore geographical and geomorphic setting. Stronger S-W waves are diffracted by Yeu Island before they reach the shoreface. Between Yeu Island, Noirmoutier Island and the mainland the bathymetry is very shallow (<15 m NGF), with a large rocky platform and complex sand bars formed principally by the ebb delta of the Fromentine inlet (Fig. 1a). In such an environment combined with the macro-tidal range, the bottom friction as well as complex refraction phenomena strongly increase with low tides (Bertin et al., 2007).

3.2. Wave conditions and water levels over the study period

The hydrodynamic context over the study period is presented in Fig. 2. It displays the significant wave height measured at 08504-buoy

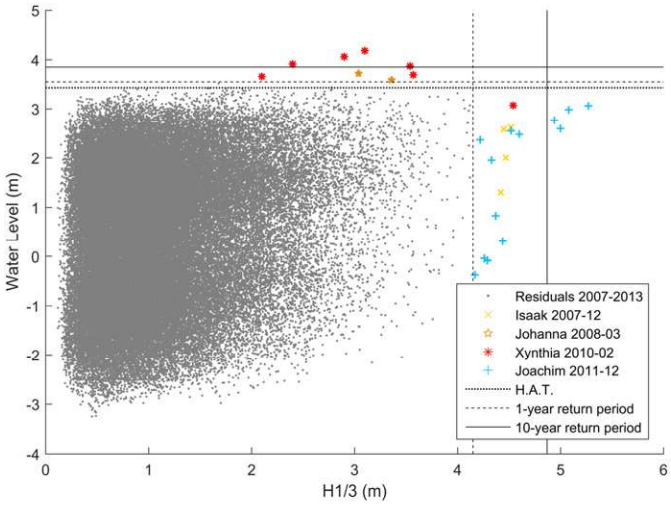

Fig. 2. Simultaneous measurements of the water level at Saint-Nazaire tide gauge (REFMAR) and the significant wave height at the 08504 Yeu buoy (CEREMA) between December 2007 and September 2013 and their respective 1-year and 10-year return periods. The Highest Astronomical Tide (H.A.T.) level is also represented on the figure.

located 12 km north of Yeu Island at 14 m depth, and variations in water level at the nearest tide gauge (Saint-Nazaire). The 08504-buoy is non-directional, it measures the usual wave parameters at variable rates: from hourly measurements during fair weather conditions up to every 10 min during storm conditions. The tide gauge is located in Saint-Nazaire harbor, 30 km north of the study sites. It provides water level variations every 10 min. Both datasets were merged using time as a key variable in order to retain only simultaneous measurements over the studied period from December 2007 to September 2013.

In Fig. 2, four events stand out from the rest of the measurements by exceeding at least the 1-year return period of the water level determined by the SHOM (Pineau-Guillou et al., 2012) and/or the significant wave height determined by the CEREMA. Three of these notable events, represented with a cross, a star and an asterisk in Fig. 2 (Isaak in December 2007, Johanna in March 2008, and Xynthia in February 2010), belong to the first period of analysis between winter 2007–2008 and August 2010. Only one event, represented with a plus sign in Fig. 2 (Joachim in December 2011), belongs to the second period between August 2010 and September 2013.

Storm Xynthia is the only event that exceeds at least the 1-year return period of both the water level and wave height but not simultaneously. Due to a large storm surge, the water level even exceeded the 10-year return period. On the contrary, Storm Joachim exceeded the 10-year return period of the significant wave height without reaching abnormally high water levels.

Based on the Dolan and Davis (1992) storm classification, Storms Isaak and Johanna belong to class IV (severe) with a Storm Power Index (SPI) reaching 2247 and 2036, respectively, just below the threshold (2322) of the next extreme class. Storms Xynthia and Joachim belong to class V (extreme) with an SPI reaching 3462 and 3721, respectively, below the average score (4548) of the Dolan and Davis (1992) 42-year period of analysis. Based on the maximum significant wave height and the duration of the storm, the Dolan and Davis (1992) classification gives a good assessment of a storm's intensity and its potential destructive power. However, in a macro-tidal environment, the concomitance of high spring tide levels with the peak of the storm enhances the potential destructive power and the erosional response of the beach (Short, 1991; Zhang et al., 2001; Ruz and Meur-Ferec, 2004; Esteves et al., 2012). The Dolan and Davis (1992) classification does not take into account this phenomenon. During the first period of analysis, Storms Johanna and particularly Xynthia strongly impacted the study sites by reaching high water levels and ordinary (<1-year return period for Johanna) to uncommon (>1-year return period for Xynthia) wave heights during storms. Both peaks of the storm surges occurred during a high spring tide (Fattal et al., 2010; Bertin et al., 2014). The water levels were high enough to pass over the highest astronomical tide level (3.43 m NGF) causing significant geomorphic changes on the beaches. In fact, the abnormally high water levels reached during a storm event, i.e. the storm tide, is the most important factor in beach erosion potential compared to wave energy (Dean, 1991; Zhang et al., 2001). As an example, strong waves exceeding the 10-year return period were recorded during Storm Joachim (during the second period of analysis) but the storm occurred during neap tides and the measured water level remained below the 1-year return period, which limited the damage in the study area. Moreover, strong bottom friction occurs at low water levels, which dissipates much of the wave energy.

Of the four events, Storm Xynthia is remembered as the most destructive: during the night of the 27th to the 28th of February 2010, 47 people died in France and material damages were estimated at >2 billion euros. The wind came from the SW sector with gusts reaching 36 m/s (Creach et al., 2015). The sea-level pressure dropped to 977 mbar (Bertin et al., 2014). At the peak of the storm, the spring tide was high and the significant wave height reached >3.5 m at the buoy between Yeu Island and Noirmoutier Island. Wave height measurements were not exceptional during Storm Xynthia (Fig. 2), nor were wind measurements whose wind speed values were lower than several storms over the last 15 years that produced gusts of over 50 m/s (Bertin et al., 2015). On the contrary, Xynthia generated a large storm surge ranging from 1 m above the astronomical water level prediction in Saint-Nazaire, 30 km north of the study sites, to 1.25 m in Les-Sables-d'Olonne, 45 km south of the study sites (Bertin et al., 2012). This exceptional storm surge is explained by the unusual track of the storm from the SW to the NE part of the Bay of Biscay (Rivière et al., 2012), generating young and steep waves enhancing surface stress (Bertin et al., 2015). The return period associated with the high water levels observed during Xynthia exceeds 100 years in Saint-Nazaire and Les Sables-d'Olonne tide gauges (Pineau-Guillou et al., 2012).

The two periods, defined by the three dates of LiDAR surveys, differ in terms of the number of extreme events. The earlier period (May 2008–August 2010) has much greater potential for eroding the coast due to the concomitance of high spring tide levels with the peak of the storms, unlike the second one (August 2010–September 2013) which is more favorable for the resilience of the coastal system (Thom and Hall, 1991). The earlier period will be referred in the text as “period 1”, and the later period as “period 2”.

4. Materials and methods

To explore how the beach dune system has changed between each LiDAR survey, a methodology based on DEM differencing and shoreline migration is applied. First, the characteristics of the LiDAR measurements are presented, and the pre-processing of the datasets is also detailed. Accounting for the different morphologies of the beaches and dunes between the study sites, a methodology is developed to extract two geomorphic features: the dune base (Dlow) and the dune crest (Dhigh). These limits and the mean high water level (MHWL) are used to spatially segregate results of the DEM differencing. To infer geomorphological changes observed between two DEMs, we needed to distinguish those significant variations in the topography of the beach from those small variations that may be attributed to noise inherent to LiDAR data. A methodology outlined by Wheaton et al. (2010) is applied to deal with this geomorphic change detection problem, to produce reliable erosion and deposition maps and sediment budgets. Finally, the time series of the extracted dune base are used to estimate the shoreline mobility accounting for its horizontal and vertical movements. The procedure is applied to the three study sites for periods 1 and 2. The main steps of the procedure are summarized in Fig. 3.

4.1. LiDAR measurements

4.1.1. LiDAR survey characteristics

The 2008 dataset was acquired during the GERRICO program airborne survey using an Airborne Laser Scanning (ALS) LiDAR system providing a 3D point cloud of 3 points per m^2. This campaign took place between 4th and 7th May 2008 over the western French coast and was conducted by the private company ACTIMAR (France). The altimetric accuracy for this acquisition is higher than 0.15 m, and the planimetric accuracy is <1 m.

The 2010 dataset used in this study comes from the Litto3D project providing topographic and bathymetric data of French coastal areas (Pastol, 2011). The data were acquired by the SHOM and the French National Geographic Institute (Institut Geographique National - IGN) using both topographic and bathymetric LiDAR. These data were acquired on 28th and 29th August 2010. The Litto3D LiDAR data have an altimetric accuracy of nearly 0.2 m associated with a planimetric accuracy estimated at <1 m, and a density of 3 points per m^2.

The 2013 LiDAR data were acquired on 23rd September 2013 using an ALS70-HP LiDAR system flying at 2500 m. The processed point cloud has a 6 pts/m^2 density (Ba et al., 2015) with a planar accuracy of ~0.15 m and an altimetric precision of ~0.1 m. The overall processing

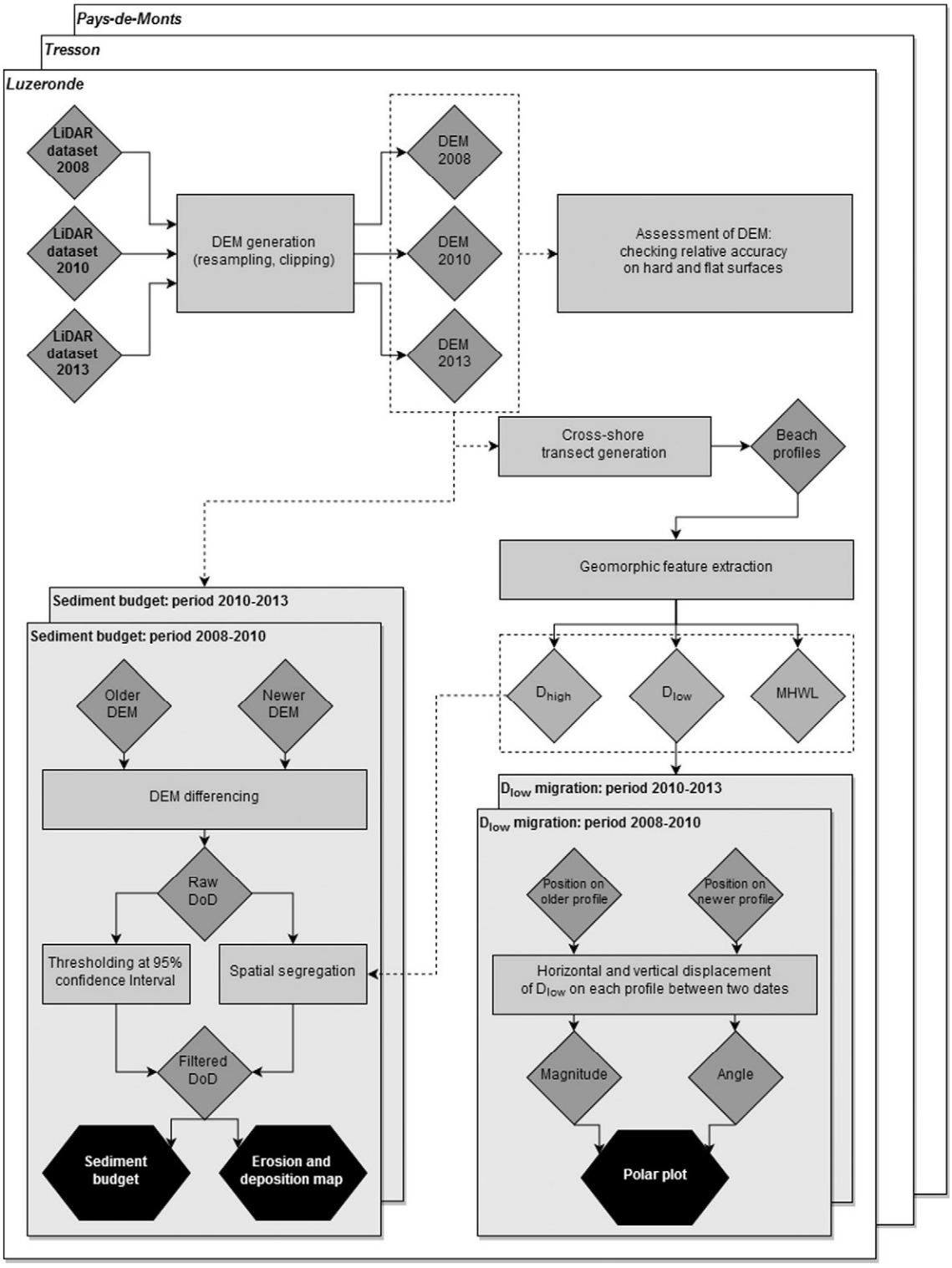

Fig. 3. Flow chart of the main steps and processing of the methodology used in this paper.

of this survey was carried out by the private company FIT-Conseil (France).

4.1.2. Pre-processing of LiDAR datasets

Each point of the 3 datasets corresponds to discrete return ALS data. For this study, only the last return corresponding to the background is kept. The 3 datasets were provided as "bare earth" model as the vegetation and the buildings were already removed. The 3 datasets are overlapped and clipped in order to determine an area common to the three surveys for each site. Then, each dataset is resampled on the same grid delimited by the common area at 1 m cell resolution using the nearest neighbor method. According to the recommendations of Woolard and Colby (2002), the 1 m resolution is the most suitable for volumetric change calculation and detailed representation of dune morphology. Finally, only the beach and dune area are extracted. Urbanized areas, forest stands, swamp and sea are

excluded from the datasets using photo-interpretation from available orthophotographs.

4.1.3. Assessment of LiDAR datasets

In order to detect significant elevation change between two surveys, the relative vertical accuracy between the compared DEMs is more important than the absolute vertical accuracy estimated by comparing each survey to ground control points at higher accuracy (Zhang et al., 2005). The three LiDAR datasets are compared to check their consistency between each other. Regions of interest are defined on hard and flat areas like parking lots and large roads as suggested by Zhang et al. (2005). An RMS error is calculated on a cell-by-cell basis. The relative accuracy represented by the mean RMSE including every dataset and study site is about 0.09 m with a standard deviation of 0.04 m (Table 2), which is below the estimates of relative accuracy (Zhang et al., 2005; Young and Ashford, 2006) and absolute accuracy (Krabill et al., 2000; Sallenger Jr. et al., 2003) found in the literature.

4.2. Extraction of geomorphic features

Transects are generated perpendicular to the coast shape along the study sites at 50 m spacing. Based on transects, topographic beach profiles are extracted from LiDAR datasets. A total of 39 profiles were extracted for the Luzeronde site, 59 for the Tresson site and 113 for the Pays de Monts site. In this study, a profile by profile analysis was used in order to extract the Mean High Water level (MHW), the dune base (D_{low}) and the dune crest (D_{high}). The MHW level is a feature simply extracted by intersecting each beach profile with the contour line $z = 1.88$ m NGF. D_{low} and D_{high} are identified using the first derivative (slope) and curvature of the beach profile z. The dune crest (D_{high}) is a feature corresponding to a high negative curvature value associated with a high elevation value. Since there may be multiple candidates for the dune crest location, the detection was thresholded to 9 m for the Luzeronde and Tresson sites and 5 m for the Pays de Monts site, meaning that the dune crest (D_{high}) cannot be lower than these values. The dune base (D_{low}) is described as a high positive curvature value associated with a sudden slope increase. In order to make the dune base (D_{low}) extraction easier on the complex morphologies of the sites investigated, the dune base (D_{low}) was searched for only between the beginning of the profile and the cross-shore location of the dune crest (D_{high}) for all the sites.

The first derivative of the elevation is defined as follows:

$$z' = \frac{dz}{dx} \tag{1}$$

where dx is the 1 m sampling.

The curvature can be written as:

$$k = \frac{z''}{\left(1 + z'^2\right)^{3/2}} \tag{2}$$

where z' is the first derivative and z'' the second derivative, described as:

$$z'' = \frac{d^2 z'}{dx^2} \tag{3}$$

Since LiDAR data record small-scale topographic variations, important features such as the dune base (D_{low}) and dune crest (D_{high}) might be mislocated due to topographical noise. Filtering is needed to locate the significant elevation changes on the first derivative and curvature functions, disregarding the elevation profile noise. In order to retrieve the features successfully, a space-scale approach (Witkin, 1984) is used here following a method detailed in Gao (2009). A Gaussian kernel filter smooths the LiDAR-derived profiles z and keeps the most significant information. The standard Gaussian distribution $G(x)$ is defined as:

$$G(x, \sigma) = \frac{1}{\sqrt{2\pi}\sigma} exp\left(-\frac{x^2}{2\sigma^2}\right) \tag{4}$$

where x is the designated variable and σ its standard deviation. The smoothed profile $F(x) = Z$ is obtained by convoluting the original LiDAR elevation profile $f(x) = z$ as follows:

$$F(x, \sigma) = f(x) * G(x, \sigma) \tag{5}$$

where $G(x, \sigma)$ is the Gaussian kernel and "*" symbolizes the convolution. For all the sites studied, $\sigma = 3$ was used as well as a kernel window of $[-5, 5]$ (m) (Fig. 4). When the beach profile z was smoothed, the slope and the curvature of the profile were computed.

As the automated extraction of the dune base (D_{low}) and dune crest (D_{high}) is based on a number of assumptions, manual editing is needed to check the consistency of their positions (Stockdon et al., 2009).

4.3. Efficiency of beach feature extraction

The efficiency of the automatic extraction of the dune crest (D_{high}) and the dune base (D_{low}) were assessed by visually checking their respective position on every beach profile of the study sites (Fig. 5). In a few cases when the position was wrong, it was necessary to edit to the correct position manually (Table 1). For the dune crest, errors were usually found where blow-outs are present (Tresson and Pays-de-Monts sites) or where the foredune is backed by higher back dunes (Pays-de-Monts site). In the case of the dune base, manual editing of its position was more often needed in the 2013 DEM because of a smoother topographic break between the beach and the dune on the profile and the building embryo dunes, both associated with the recovery of the system, leading to a potential error in the determination of the position of the dune base. On the contrary, few errors were found for the extraction of the dune base in the 2010 DEM because of the sharp dune undercutting likely associated with Storm Xynthia's impact (Fig. 1b–d).

Unfortunately, no field data are available to validate the consistency of the extraction procedure. Therefore, despite the high accuracy of the RTK-dGPS, the delineation of the dune base and the dune crest can also be subject to the interpretation of the operator during field surveys. Moreover, as demonstrated in Palaseanu-Lovejoy et al. (2016) and Rutzinger et al. (2012), manual digitizing of geomorphological breaklines on a DEM has a lower precision and is not identically reproducible (it varies between operators) compared to automatic extraction, even with manual editing of uncertain segments.

A recent attempt to find a robust alternative methodology to the Least Cost Path extraction and the Curvature approach was presented

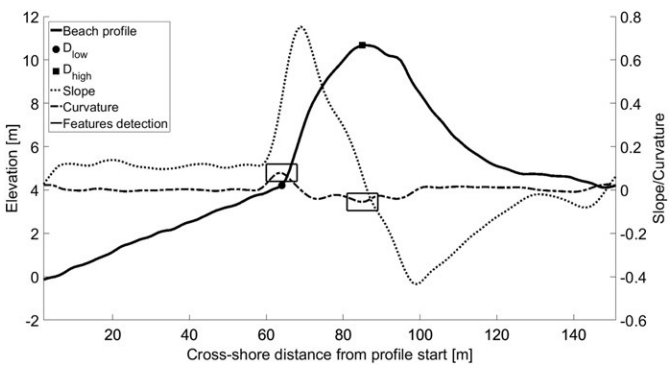

Fig. 4. Dune base (D_{low}) and crest (D_{high}) detection from beach profile using slope and curvature with $\sigma = 3$ and a $[-5, 5]$ (m) kernel.

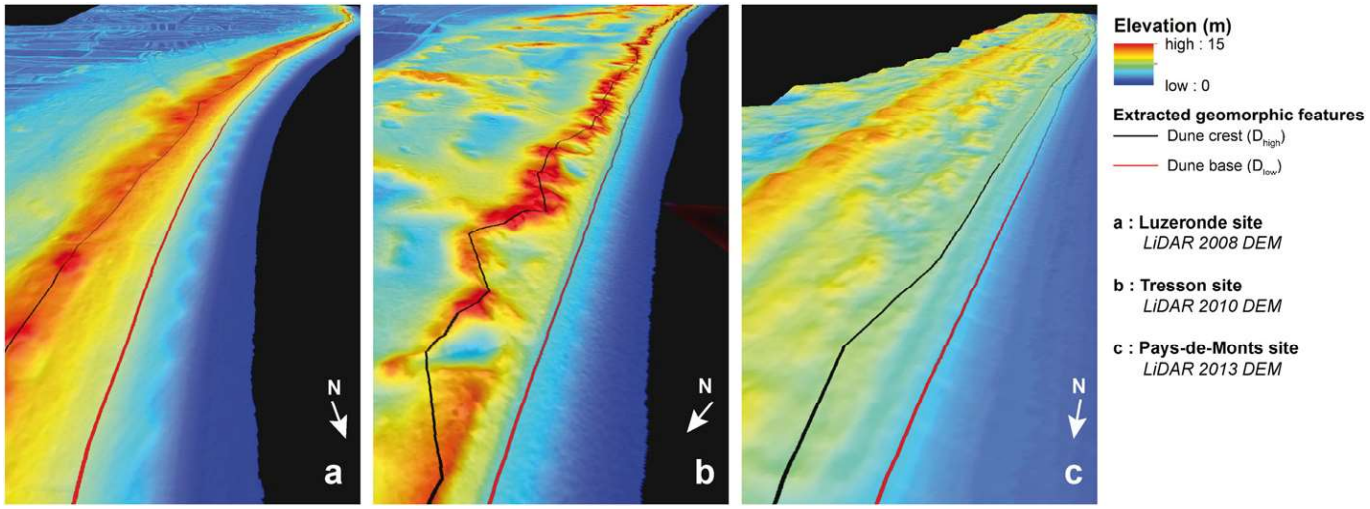

Fig. 5. Oblique view of the DEMs of the three sites with the interpolated lines of the extracted dune base (D_{low}) and dune crest (D_{high}). This figure is available in colour online at https://www.journals.elsevier.com/geomorphology.

by Palaseanu-Lovejoy et al. (2016). Although the procedure was developed on sea cliff transects, it seems robust enough to be applied to a smoother dune relief. Further investigations are needed to compare the three procedures on various beach-dune morphologies.

4.4. Geomorphic change detection

4.4.1. DEM differencing principle

Two DoDs (DEMs of Difference) are computed by subtracting the elevation values of the more recent DEM from the older ones on a cell-by-cell basis such that areas of erosion are expressed negatively, and areas of deposition positively. Volumetric change is also calculated from the DoD through the sediment budget. It is classified into three categories: erosion, deposition and net change, which is the balance between erosion and deposition. Volume changes per unit surface ($m^3\ m^{-2}$) are computed to compare volumetric results with each other between and within study sites despite differences in the spatial extent.

The first DoD covers the 2008–2010 period from the beginning of May 2008 to the end of August 2010 (≈2.5 years). The second DoD covers the 2010–2013 period from the end of August 2010 to 23rd September 2013 (≈3 years).

4.4.2. Uncertainty in DEM differencing

The vertical absolute accuracy of LiDAR surveys used to quantify beach change is generally about ±0.15 m (Sallenger Jr. et al., 2003).

Table 1
Quality of the dune base and crest detection per site per year.

Feature extracted	Dune base			Dune crest		
Year	2008	2010	2013	2008	2010	2013
Luzeronde						
Manually edited points	16	2	5	0	0	0
Number of points	39	39	39	39	39	39
Auto-detection rate (%)	59	95	87	100	100	100
Tresson						
Manually edited points	2	0	20	3	5	4
Number of points	59	59	59	59	59	59
Auto-detection rate (%)	96.6	100	66.1	94.9	91.5	93.2
Pays-de-Monts						
Manually edited points	8	11	55	8	12	17
Number of points	113	113	113	113	113	113
Auto-detection rate (%)	92.9	90.3	51.3	92.9	89.4	85

Considering this potential error, the probability of a hard structure (road, building, topographic benchmark, etc.) showing no change in a DoD is very small. The elevation change values are normally distributed with many small change values represented around zero. There is uncertainty about whether this large number of small changes is real or due to error measurements. The interpretation of small changes in elevation is difficult because of the inherent noise induced by error measurement. A detection threshold is applied to the DoD to distinguish meaningful geomorphological changes from such uncertain elevation change values.

Based on the assumption that inherent errors in the datasets are independent, the first step in determining a reliable detection threshold is to propagate the error of the two surface models used to compute the elevation difference (Taylor, 1997; Brasington et al., 2003):

$$\delta_{DoD} = \sqrt{(\delta z_{new})^2 + (\delta z_{old})2} \tag{6}$$

where δ_{DoD} is the propagated error of the DoD, δz_{new} the individual error of the most recent DEM, and δz_{old} the individual error of the older one. In this study, post-processed LiDAR surveys were exploited and variable estimates of the uncertainty (δz) were not available. Each dataset has different reported vertical uncertainties ranging from ±0.1 m to ±0.2 m but they are uniform between the study sites (Table 2). Consequently, the combined error (δ_{DoD}) of the independent uncertainty of each DEM is uniformly applied to the entire DoD.

The second step is to determine the significance of the propagated uncertainty of the DoD. Assuming that the estimate of δz is a reasonable approximation of the standard deviation error (σ) and based on Eq. (1), the threshold is specified at a user-defined confidence interval:

$$U_{crit} = t\left(\sqrt{(\sigma_{new})^2 + (\sigma_{old})2}\right) \tag{7}$$

where U_{crit} is the critical threshold error below which elevation changes will be considered noise, σ_{new} the individual error of the most recent

Table 2
Uniform vertical accuracy of each LiDAR dataset provided by the surveyors.

Dataset	Vertical accuracy (≈σ)
2008	±0.15
2010	±0.20
2013	±0.10

Table 3
Comparison of detection thresholds based on RMSE calculated on hard flat surfaces and on the probabilistic approach at a 95% confidence interval.

Study site	DoD: 2008–2010		DoD: 2010–2013	
	RMSE	95% CI	RMSE	95% CI
Luzeronde	±0.06	±0.49	±0.13	±0.43
Tresson	±0.05	±0.49	±0.04	±0.43
Pays-de-Monts	±0.13	±0.49	±0.14	±0.43

surface model, σ_{old} the individual error of the older one, and t the critical t-value at the given confidence level.

As in Wheaton et al. (2010), the 95% confidence interval is used as a critical threshold. Following this method, elevation changes that have a 95% chance of not being due to error measurement are considered meaningful. The cells whose elevation change is below this confidence interval are excluded from the analysis and considered too uncertain to be computed in a sediment budget or to allow inference of geomorphological processes. The two uniform detection thresholds at a 95% confidence interval are calculated between the 2008 DEM and the 2010 DEM, and between the 2010 DEM and the 2013 DEM, respectively. It is consequently uniform between the three study sites (Table 3).

4.4.3. Segregation of geomorphic change detection

The extracted beach features (D_{high}, D_{low}, and MHW) are finally used to segregate the results obtained from the DoDs as limits of four cross-shore zones representing interconnected subsystems of the beach and dune system. The first zone is the tidal beach: it lies between the seaward beach limit covered by the DEM and the mean high water level (MHW). The second zone is the upper beach between the MHW and the extracted dune base (D_{low}). The third zone is the foredune between the extracted dune base (D_{low}) and the extracted dune crest (D_{high}) (Fig. 6). The forth zone covers the back dune from the frontal dune crest (D_{high}) to the landward limit of the resampled DEM. A fifth zone named "unclassified" is also delimited. It includes portions of the DEM where the cross-shore transects cannot be computed. These unclassified zones are generally located at the edges of the DEM. The limits of the zones may vary between each survey due to elevation change on the beach. In the DoDs, the limits of the older DEM are considered in the calculation of surface and volumetric changes.

Tools provided by ArcGis 10.2.2 are used to collect and transform the datasets. The Geomorphic Change Detection software 6.1.10 (http://gcd.joewheaton.org), developed in Wheaton (2008), is used to build the DoDs, take into account their respective uncertainties, and compute sediment budgets and segregations.

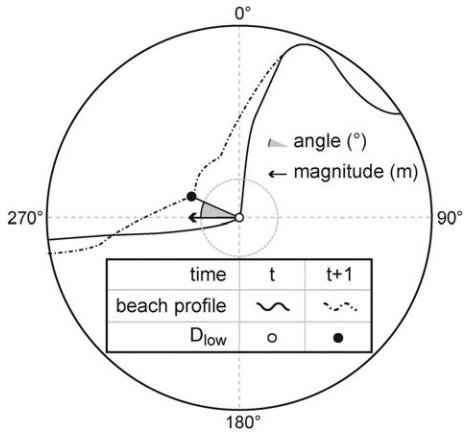

Fig. 7. Schematic polar plot of the dune base (Dlow) migration index between two theoretical beach profiles. The centre of the polar plot represents the position of D_{low} on the earlier profile (t). The position of D_{low} on the later profile (t + 1) is defined by a distance (magnitude) and an azimuth (angle) relative to the initial position of D_{low} on the earlier profile (t).

4.5. Dune base (D_{low}) migration index

The shoreline mobility is assessed through the creation of a new index resulting from the combination of the horizontal and vertical movements of the D_{low} feature. This index, computed for each transect, is composed of the horizontal distance and the angle between the positions of D_{low} between two consecutive dates on each transect. The shoreline mobility is then projected onto a polar plot representing the migration of the extracted points in a given period (Fig. 7). The magnitude of the polar plots in the Results section is presented with a logarithmic scale in order to enhance differences between the points.

5. Results

The volumetric results presented in the following sections do not include unclassified areas, except for the Pays-de-Monts site.

5.1. Luzeronde

5.1.1. Geomorphic change detection

Between 2008 and 2010, the sediment budget of Luzeronde beach is approximately balanced with a very slight loss of sand made uncertain by an error volume that affects both positive and negative net changes (Fig. 8a, b and Table 4). In fact, erosion and deposition occur

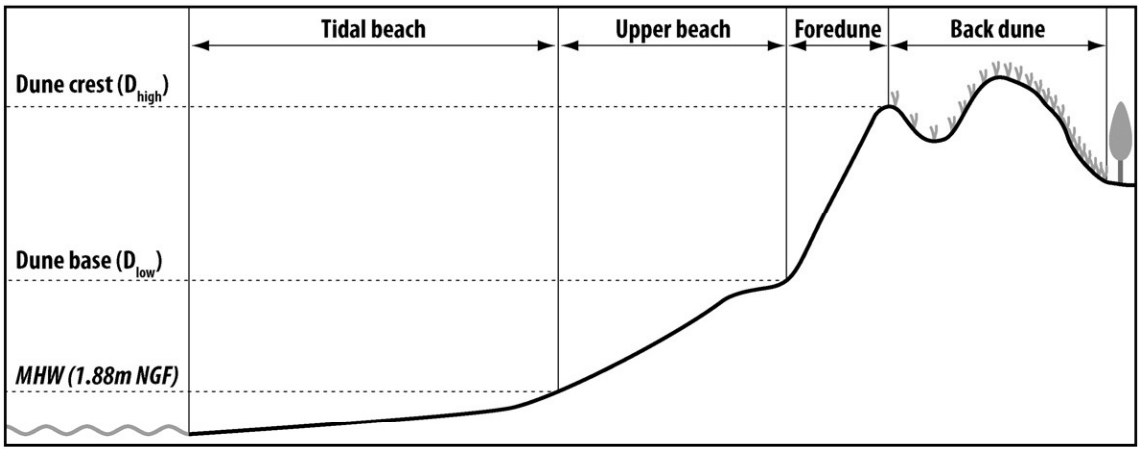

Fig. 6. Beach segregation displayed on a cross-shore profile based on datum (MHW) and extracted geomorphological features (dune base and dune crest).

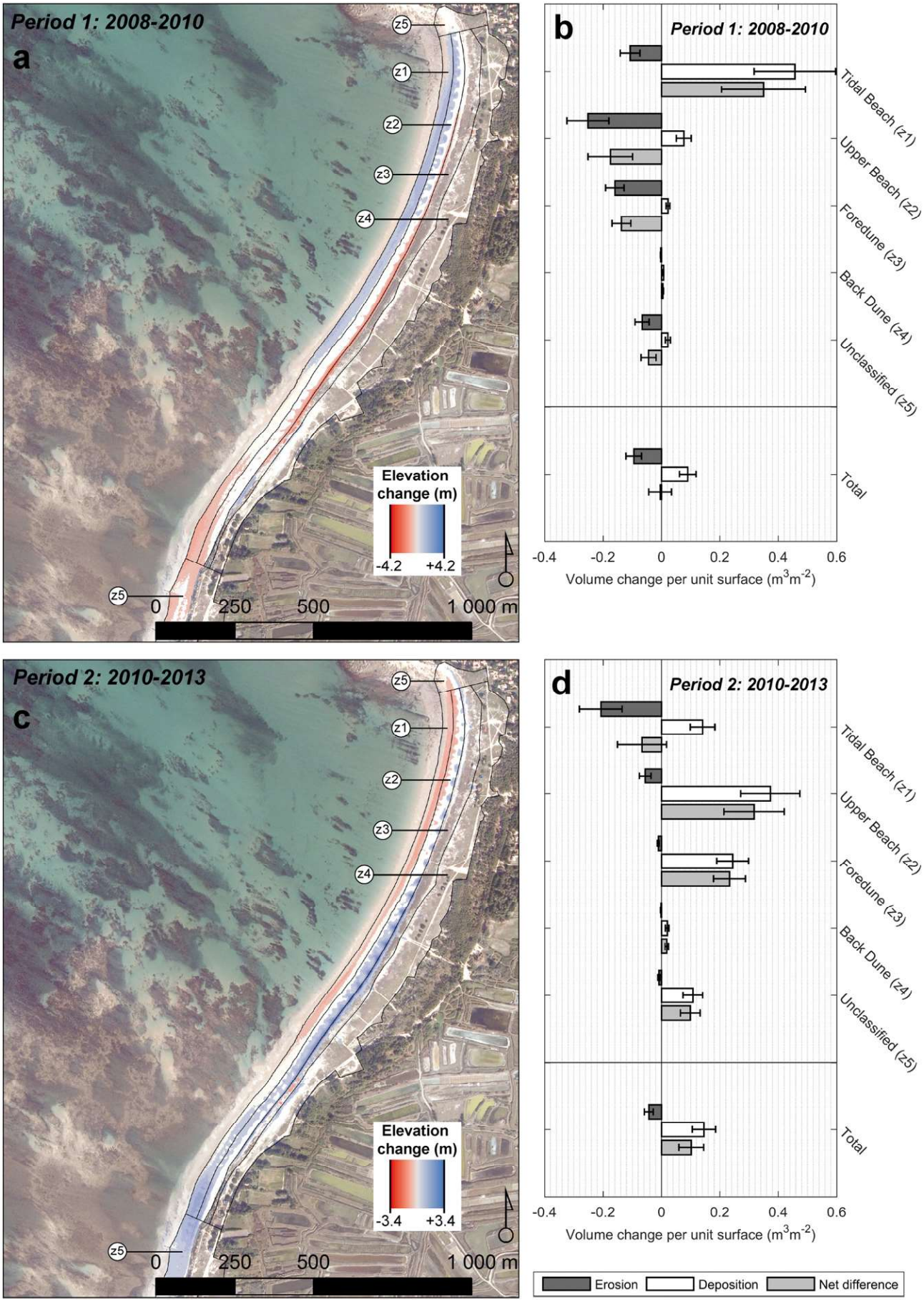
Period 1: 2008-2010
a
z5
z1
z2
z3
z4
Elevation change (m)
-4.2
+4.2
0
250
500
1 000 m
b
Period 1: 2008-2010
Tidal Beach (z1)
Upper Beach (z2)
Foredune (z3)
Back Dune (z4)
Unclassified (z5)
Total
-0.4
-0.2
0
0.2
0.4
0.6
Volume change per unit surface (m3m-2)
Period 2: 2010-2013
c
Elevation change (m)
-3.4
+3.4
d
Erosion
Deposition
Net difference

at about the same magnitude. However, deposition mainly occurs on the tidal beach (79% of the total volume of deposition), while erosion mainly occurs on the upper beach and the foredune (50% and 29%, respectively, of the total volume of erosion) (Table 4). Nonetheless, the tidal beach shows the most significant evolution with a net volume change per unit surface reaching 0.35 $m^3\ m^{-2}$, including 0.45 $m^3\ m^{-2}$ of deposition and 71% of grid cells showing significant changes within this zone (Fig. 8a). Furthermore, deposition is principally visible on the northern part of the beach, while erosion is visible on the southern side of the beach, with higher values from either side of the D_{low} line (Fig. 8a). Beach cusps appear on the upper beach as a deposition feature against the MHW line and as an erosion feature against the D_{low} line (Fig. 8a).

The second period of analysis is less equivocal: the sediment budget is clearly positive with 77% of deposition in the total volume difference distribution (Table 4). The spatial distribution of the significant changes follows the same pattern as in the 2008–2010 period but inversely (Fig. 8c, d). Deposition mainly occurs on the upper beach and the foredune, while erosion mainly occurs on the tidal beach. This time, the upper beach and the foredune are the zones where volume changes per unit surface are the most important especially in deposition, while the tidal beach displays more mixed results slightly dominated by erosion. Erosion is principally visible on the northern part of the beach, while deposition is visible on the southern side of the beach with higher values from either side of the D_{low} line (Fig. 8c). Beach cusps appear again on the upper beach but this time as an erosion feature against the MHW line, and as a deposition feature against the D_{low} line (Fig. 8c).

5.1.2. Migration of the dune base (D_{low})

The extracted dune base points migrate mainly in a seaward and downward direction between 2008 and 2010, whereas they migrate mainly in a seaward and upward direction between 2010 and 2013 (Fig. 9a). In fact, almost all the points of the first period are located in the lower half of the polar plot with >80% located in the quarter between 180° and 270°. On the contrary, the upper half is symmetrically occupied, with few exceptions, by most of the points of the second period (Fig. 9a), which are spread in the same way as for the first period with a similar magnitude. Some of these points show a difference by displaying a slightly downward displacement with a higher magnitude that can exceed 10 m between 2010 and 2013. Some points of the second period also show no horizontal movement but a non-significant (<1 m) to moderate upward direction (Fig. 9a).

It is clear on the 2008–2010 DoD that the dune base is eroded during this period, which corresponds to negative off-set (Fig. 8a). The polar plot gives complementary information: the dune base line (D_{low}) also predominantly migrates seaward and downward during this erosive period (Fig. 9a). This situation may be explained by a first important phase of erosion induced by Storm Xynthia which has possibly caused a landward and downward displacement of the dune base, followed by a quick recovery phase during the weeks between this storm (February 2010) and the next LiDAR campaign (August 2010). Despite a balanced sediment budget between 2008 and 2010, a lot of sand redistribution has occurred. During the possible second phase, sediment redistribution on the upper beach may have caused a seaward displacement of the dune base without reaching the altimetric level of the previous campaign (May 2008), inducing a downward displacement of the dune base and a negative offset on the 2008–2010 DoD. Such an observation has already been described in Crapoulet et al. (2017).

5.2. Tresson

5.2.1. Geomorphic change detection

During the first period of analysis, the sediment budget is obviously positive with 95% of the volume difference distribution attributed to deposition (Table 4). The remaining 5% of erosion is mainly located on the large back dune of the Tresson site (Fig. 10a), this is likely to correspond to isolated trees filtered from the 2010 bare earth model that have been provided by the IGN. Erosion marks are also visible in several blow-outs near the D_{high} line. Volume changes are the most important on the tidal beach with >0.30 $m^3\ m^{-2}$ deposited (Fig. 10b) and 49% of grid cells showing significant changes. The large deposition area is thinner in the northwestern part of the beach, whereas it becomes wider towards the head of the sand spit in the southeastern part of the beach (Fig. 10a). The deposition area overlaps the MHW limit into the upper beach zone. Some thin deposition marks are also visible on either side of the D_{low} line (Fig. 10a).

Between 2010 and 2013, the sediment budget is still positive but in a rather more modest proportion (Table 4). Erosion increases to reach 19% of the total volume distribution. Some remaining trees in the back dune, which have not been filtered from the bare earth models that have been provided, may again cause some interference. Some blow-outs are still marked by erosion (Fig. 10c). However, this increase in the erosion proportion is principally attributed to a loss of sediment along the MHW limit over both the upper beach and the tidal beach. This erosion area is located more in the northwestern part of the beach (Fig. 10c). Overall, deposition, which still dominates the sediment budget, occurs along the D_{low} line over both the upper beach and the foredune. This deposition area becomes wider towards the head of the sand spit in the southeastern part of the beach. Higher deposition values can be found along the D_{low} line and the beach cusps visible towards the south-east (Fig. 10c). The upper beach and the foredune represent the most significant deposition zones with respectively 0.35 and 0.15 $m^3\ m^{-2}$ of deposition (Fig. 10d). Moreover, 52% of the grid cells within the upper beach zone show significant changes. On the contrary, the loss of sediment from the tidal beach reaches only 0.05 $m^3\ m^{-2}$ (Fig. 10d), with only 9% of grid cells showing significant changes.

5.2.2. Migration of the dune base (D_{low})

On the polar plot, the points are quite packed into three distinctive groups with few differences between the two periods (Fig. 9b). The largest group displays a slightly downward seaward displacement between 2008 and 2010. Between 2010 and 2013, the displacement is still seaward but rather upward and more spread out with a higher magnitude exceeding 10 m. The second group shows no horizontal migration during the two periods. However, the vertical displacement is barely significant between 2008 and 2010 but reaches 1 m between 2010 and 2013. The last group displays a moderate migration in a landward direction with a more upward angle for the points of the second period compared to those of the first period (Fig. 9b).

Few significant changes occur at the dune base level in the 2008–2010 DoD, with the dune base migration remaining limited as its maximum magnitude is 4 m but almost horizontally seaward. In the 2010–2013 DoD (Fig. 10c), a continuous deposition occurs at the dune base level. The polar plot indicates that the deposition results in a horizontal seaward migration of the dune base rather than an upward increase (Fig. 9b).

5.3. Pays-de-Monts

5.3.1. Geomorphic change detection

Between 2008 and 2010, the beaches of the Pays-de-Monts site lose sand with 74% of erosion in the sediment budget (Table 4). The upper

Fig. 8. Geomorphic change detection results for the Luzeronde site: (a) 2008–2010 DoD, (b) sediment buget segregation of the 2008–2010 period, (c) 2010–2013 DoD, (d) sediment budget segregation of the 2010–2013 period. This figure is available in colour online at https://www.journals.elsevier.com/geomorphology.

Table 4
Sediment budget segregation and thresholding at 95% confidence interval by site and period.

	Volume of erosion (m^3)			Volume of deposition (m^3)			Net volume difference (m^3)		
	Raw	Thresholded	±Error	Raw	Thresholded	±Error	Raw	Thresholded	±Error
Luzeronde 2008–2010									
Tidal beach	8446	6827	2143	32,431	29,029	8875	23,985	22,203	9130
Upper beach	24,180	17,143	4887	8102	5226	1750	−16,078	−11,917	5191
Foredune	11,653	9773	1930	5989	1384	398	−5664	−8390	1971
Back dune	7038	347	116	4290	997	342	−2748	650	361
Unclassified	13,799	6705	2459	7908	2245	881	−5891	−4460	2611
Total area	**65,116**	**40,796**	**11,535**	**58,720**	**38,882**	**12,245**	**−6396**	**−1914**	**16,822**
Luzeronde 2010–2013									
Tidal beach	16,819	13,095	4604	12,043	8901	2648	−4776	−4194	5311
Upper beach	5724	3651	1315	29,471	24,496	6669	23,747	20,845	6797
Foredune	1039	695	199	25,234	15,735	3518	24,195	15,040	3524
Back dune	1055	263	95	21,521	2682	849	20,466	2418	855
Unclassified	5869	883	350	16,467	10,910	3404	10,598	10,028	3421
Total area	**30,512**	**18,592**	**6563**	**104,737**	**62,724**	**17,089**	**74,225**	**44,132**	**18,306**
Tresson 2008–2010									
Tidal beach	2179	0	0	73,292	54,054	20,197	71,113	54,054	20,197
Upper beach	659	0	0	21,320	9845	3788	20,661	9845	3788
Foredune	2125	1027	303	22,913	4966	1819	20,787	3939	1844
Back dune	16,961	2594	894	53,010	4511	1546	36,050	1917	1786
Unclassified	4142	643	169	21,690	3468	1466	17,547	2824	1475
Total area	**26,067**	**4265**	**1366**	**192,225**	**76,843**	**28,816**	**166,159**	**72,578**	**28,848**
Tresson 2010–2013									
Tidal beach	22,159	6851	2697	4462	27	13	−17,697	−6824	2697
Upper beach	8712	5400	2135	44,898	36,078	9562	36,186	30,678	9798
Foredune	2543	829	269	35,264	22,087	5327	32,721	21,258	5334
Back dune	24,433	3681	1221	37,586	4144	1254	13,154	463	1750
Unclassified	3349	747	321	24,409	10,675	3103	21,060	9928	3120
Total area	**61,196**	**17,507**	**6644**	**146,618**	**73,010**	**19,259**	**85,422**	**55,503**	**20,373**
Pays-de-Monts 2008–2010									
Tidal beach	123,394	52,711	20,065	94,202	2718	1190	−29,191	−49,993	20,100
Upper beach	36,396	27,869	5635	20,733	5066	1939	−15,664	−22,803	5959
Foredune	35,587	26,917	6251	4961	881	356	−30,627	−26,036	6261
Back dune	62,938	1552	477	4496	488	202	−58,442	−1064	518
Inlet area	84,085	26,920	6016	69,478	37,985	11,210	−14,607	11,065	12,722
Total area	**342,659**	**136,032**	**38,465**	**194,304**	**47,501**	**14,976**	**−148,355**	**−88,531**	**41,277**
Pays-de-Monts 2010–2013									
Tidal beach	87,931	9428	3762	48,590	3903	1584	−39,341	−5525	4082
Upper beach	20,295	13,625	3874	70,687	60,020	15,401	50,391	46,395	15,880
Foredune	4126	3054	837	32,992	19,708	6778	28,866	16,654	6829
Back dune	6672	1383	455	78,630	11,516	4247	71,958	10,133	4271
Inlet area	41,605	27,073	9150	196,262	136,792	34,576	154,657	109,719	35,766
Total area	**160,631**	**54,564**	**18,078**	**427,161**	**231,938**	**62,586**	**266,530**	**177,375**	**65,145**

beach and especially the foredune display the most significant changes with respectively 0.15 and 0.25 m^3 m^{-2} of erosion (Fig. 11c). The inlet and the north of the study site seem to concentrate most of the significant changes with wide zones of erosion on the tidal beach and on the upper beach characterized by higher values of elevation change (Fig. 11a). The grid cells showing significant changes represent only

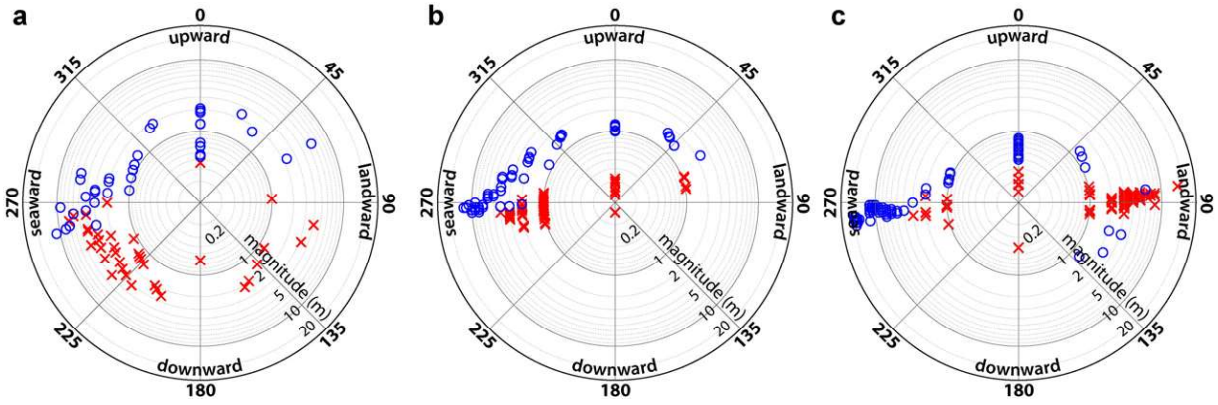

Fig. 9. Polar plots of the dune base (D_{low}) migration between 2008 and 2010 in red and between 2010 and 2013 in blue at the sites of (a) Luzeronde, (b) Tresson and (c) Pays-de-Monts.

23% within the foredune and 9% within the tidal beach. In the inlet area, zones located between the dry beach and the wet beach with high elevation change values alternate between erosion and deposition. On the upper beach, 500 m south of the high erosion values adjacent to the inlet area, a large deposition zone is located along the MHW line (Fig. 11a). Furthermore, south of this deposition zone, a thin, elongated and almost continuous strip of erosion starts in the foredune zone along the D_{low} line and continues to the southern limit of the studied area (Fig. 11a).

During the second period of analysis, the Pays-de-Monts site has a clear positive sediment budget in which 81% of the volume distribution is attributed to deposition (Table 4). The inlet area represents 58% of the total net volume difference, 50% of the total volume of erosion and 59% of the total volume of deposition, with wide areas of significant elevation changes across the dry beach and the wet beach. Apart from this particular zone, the upper beach and the foredune remain the most significant deposition zones in terms of volume changes per unit surface with, respectively, 0.30 and 0.20 $m^3\ m^{-2}$ of deposition (Fig. 11d). Moreover, 44% of the grid cells in the upper beach show significant changes. The widest areas of significant changes remain in the northern part of the study site (Fig. 11b). South of the inlet, a zone on the upper beach that shows noticeable erosion in 2008–2010 is still marked as a negative elevation change, while further south the deposition zone of 2008–2010 becomes wider with higher values of positive elevation change (Fig. 11b). The elongated and almost continuous zone of erosion, which displays uniform erosion in the first period, becomes wider in the second period, with a uniform positive elevation change this time, which overlaps the upper beach zone across the D_{low} line (Fig. 11b).

The back dune represents notably 12% of the total volume of deposition between 2010 and 2013 (Table 4). This is likely explained by the aeolian redistribution onshore of washovers caused by Storm Xynthia and visible in the central part of the study site in Figs. 11 and 12.

The inlet area strongly influences the overall sediment budget of the North Pays-de-Monts site (Table 4). To illustrate this point, if we exclude this particular area from the sediment budgets, the negative net change of the 2008–2010 DoD would increase by 11% towards erosion, while the positive net change of the 2010–2013 DoD would be divided by 2.5 (−160%) reducing the resultant deposition (Table 4). The northern part of the study site, including the inlet area, is characterized by an alternation of erosion and deposition on the upper beach. Their location does not vary notably between the two periods, although erosion tends to cover a larger area during the 2008–2010 period as well as deposition during the 2010–2013 period (Fig. 11a, b). These significant changes may be largely attributed to the inlet's specific dynamics and processes. For the rest of the beach, significant changes are principally observed at the dune base level: the foredune is uniformly eroded between 2008 and 2010, and largely recovers between 2010 and 2013 by building an embryo dune where space was left by the erosion of the first period.

5.3.2. Migration of the dune base (D_{low})

On the polar plot, the migration occurs in two opposite directions in the two periods (Fig. 9c). Between 2008 and 2010, the majority of the points are packed in an almost horizontal but slightly upward landward direction around 90°, with a magnitude generally below 10 m with one exception almost reaching 20 m. Between 2010 and 2013, most points are also packed around the horizontal line but in the opposite downward, seaward direction. The magnitude is higher than in the first period, as several points exceed 10 m and some of them reach a displacement of 20 m between 2010 and 2013. Some of the points of both periods show no horizontal displacement and a small upward movement with higher magnitude in the second period. In both cases, a few points migrate in the opposite direction of the majority of the points of their respective period with a more spread out pattern between 2010 and 2013 as their angle extent lies between 45° and 135°.

South of the inlet, the beach response at the dune base level is reversed: erosion between 2008 and 2010, and deposition between 2010 and 2013. It is as obvious in the DoDs (Fig. 11) as in the polar plot (Fig. 9c). The migration of the dune base is also horizontal in either way.

6. Discussion

6.1. Mechanisms controlling beach responses

6.1.1. Comparison of the beach response between the three study sites

Despite site-specific mechanisms, similar observations can be made between the three study sites. Between 2008 and 2010, more sediment is either deposited or eroded on the lowest part of the beach (i.e. the tidal beach), whereas between 2010 and 2013 more sediment is deposited on the upper parts of the beach (i.e. the upper beach and the foredune) (Figs. 8, 10, 11). Thus, the dune base migrates mostly in a seaward direction between 2010 and 2013, whereas it shows a more diverse and limited behavior between the sites during the first period of analysis, likely associated with storms (Fig. 9). Migration occurs at a higher magnitude during the second period than between 2008 and 2010. Moreover, the highest magnitudes in a seaward direction during the second period of analysis always display a horizontal to slightly downward direction (Fig. 9). The impact of a sequence of storms on a beach and dune system is difficult to (i) anticipate because of both site-specific geomorphological conditions and storm characteristics (Coco et al., 2014; Masselink et al., 2016; Scott et al., 2016), (ii) ascribe due to the frequency and timing of the LiDAR surveys relative to the storm events. Therefore, the beach responses during the recovery phase appear to be more homogenous between the three study sites.

The three study sites show different morphological responses to either period 1 (2008–2010) and period 2 (2010—2013). Site-specific conditions can explain the differences in the redistribution of sand within and between each study site as well as local factors that can influence sand supply (cf. Hesp, 2002). Along the SW coast of England, pre- and post-storm LiDAR surveys showed highly variable beach responses to the impact of 2013/14 winter storms and recovery, principally due to the embayed morphology of the coast associated with a variable beach orientation (Masselink et al., 2016; Scott et al., 2016; Burvingt et al., 2017).

6.1.2. Luzeronde

During the two consecutive periods of analysis, both accretionary and erosive responses are observed showing a symmetrical cross-shore and alongshore sediment redistribution within the embayment (Figs. 8, 9a). The two rotations of the beach were dominated by an almost balanced combination of alongshore and cross-shore sand redistribution around a fulcrum point (Harley et al., 2015). Luzeronde beach is characterized by a W-NW orientation. Although the temporal resolution of the LiDAR surveys prevents us from attributing the observed changes to any storm, we can assume that the SW wave approach of Storm Xynthia, oblique to the shoreline, was likely to cause a rotation of the beach with significant erosion along the southern (up-wave) part of Luzeronde beach while deposition could occur in the opposite northern (down-wave) part of the beach (Fig. 8). As described in Section 3.1, the most frequent and less energetic waves come from the W-WNW and WSW-W sectors. Although Storm Joachim showed larger waves than the most frequent ones (Fig. 2), its direction was similar (Bertin et al., 2015). This more dominant westerly wave forcing is likely to cause a counter-rotation of the beach. The periodic rotation of embayed beaches has been observed worldwide at various time scales depending on variations in wave forcing from a single storm event to climate oscillation (Ranasinghe et al., 2004; Thomas et al., 2012; Turki et al., 2013; Harley et al., 2015).

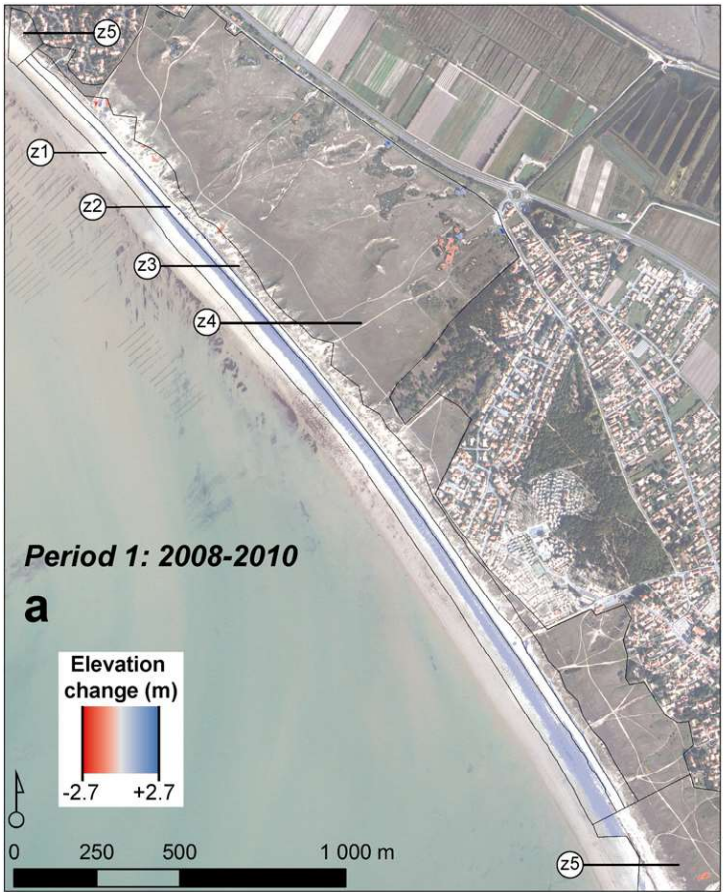
z5
z1
z2
z3
z4
Period 1: 2008-2010
a
Elevation change (m)
-2.7
+2.7
0
250
500
1 000 m
z5

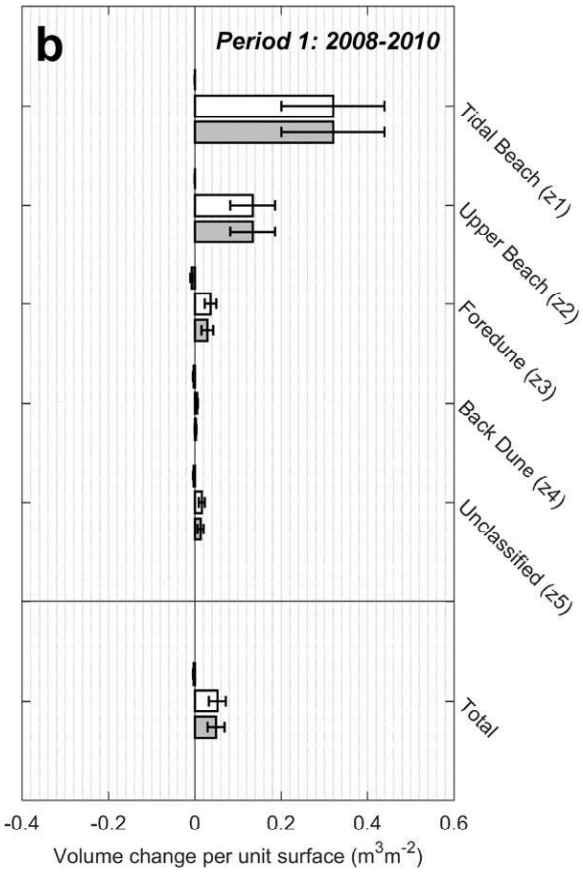
b
Period 1: 2008-2010
Tidal Beach (z1)
Upper Beach (z2)
Foredune (z3)
Back Dune (z4)
Unclassified (z5)
Total
-0.4
-0.2
0
0.2
0.4
0.6
Volume change per unit surface (m3m-2)

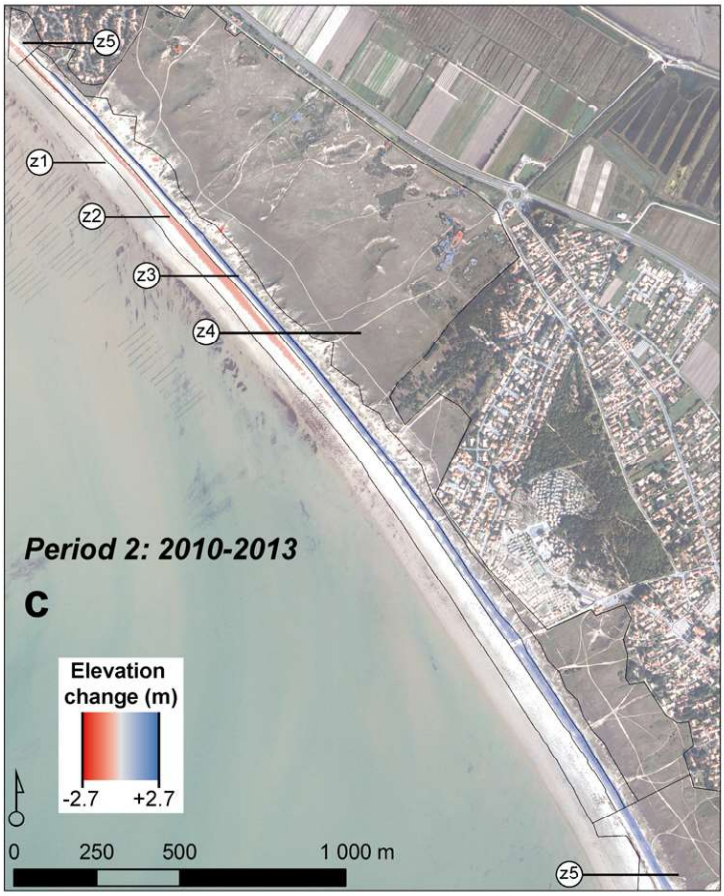
z5
z1
z2
z3
z4
Period 2: 2010-2013
c
Elevation change (m)
-2.7
+2.7
0
250
500
1 000 m
z5

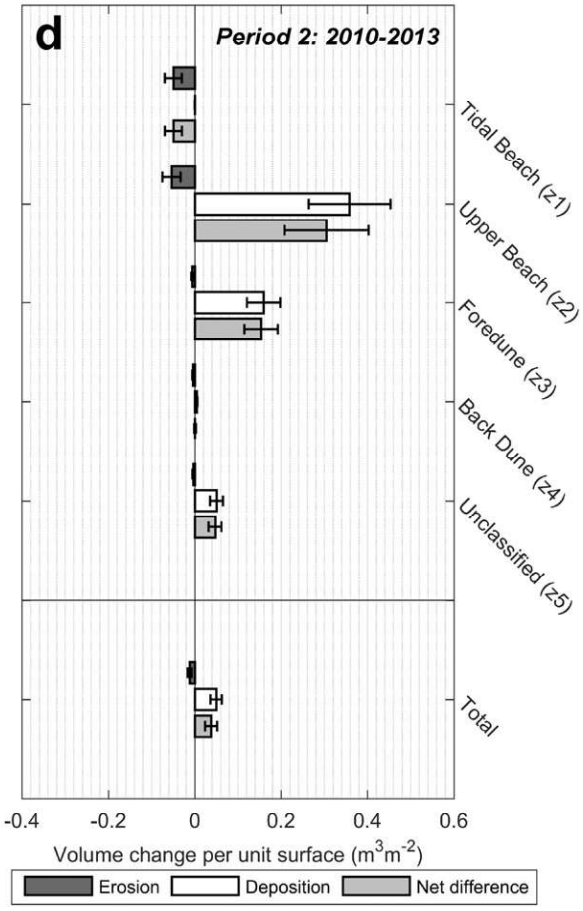
d
Period 2: 2010-2013
Tidal Beach (z1)
Upper Beach (z2)
Foredune (z3)
Back Dune (z4)
Unclassified (z5)
Total
-0.4
-0.2
0
0.2
0.4
0.6
Volume change per unit surface (m3m-2)
Erosion
Deposition
Net difference

The beach is sheltered by two headlands (Fig. 1a) that probably limited the loss of sediment from the system, which stayed in relative equilibrium (Fig. 8). Moreover, as described in Scott et al. (2016), high-energy events are sometimes required for the recovery of beaches; sediments may remain on the subtidal beach until long swells mobilize them, transporting them onshore. Sediment input to the beach could be explained by the longer swell of Storm Joachim. Indeed, due to high water levels, storms Johanna and Xynthia probably eroded the upper beach and the foredune. Some of the eroded sediment were likely to be deposited on the tidal beach, or further offshore on the subtidal beach. These The longer swell of Storm Joachim, with a peak period reaching 15 s (Bertin et al., 2015), may have mobilized sediments again providing input to the beach. Unfortunately these hypotheses can only be verified with pre- and post-storm surveys.

6.1.3. Tresson

The SW wave approach of Storm Xynthia was nearly perpendicular to the shoreline of Tresson beach. The subtidal beach is very shallow, flat and wide; for instance, the distance between the dune base and the −5 m contour can exceed 3 km (Fig. 1). Even though the peak period of the wave didn't exceed 10 s during the storm surge, a large amount of sediment may have been mobilized and transported onshore, if so, this phenomenon could be an input of sediment to the beach. Indeed, limited movement of the dune base (D_{low}) is observed between 2008 and 2010 (Fig. 9b). The upper beach and the dune base were not severely affected during period 1 (Fig. 10a), although it is characterized by a higher prevalence of storm events. The erosion of the headlands north of the study site may also have provided sediment to the sand spit.

The sand supply brought onto the tidal beach during the period 1 was probably transported onto the upper beach during the period 2 by mechanisms dominated by aeolian processes as described in Ruz and Meur-Ferec (2004) and Suanez et al. (2012). Sediments are redistributed alongshore in the direction of the head of the sand spit mainly by wave processes(Evans, 1942; Héquette and Ruz, 1991; Davis and FitzGerald, 2004). Hydrodynamic conditions are characterized by a more westerly approach during period 2 (see Section 3). The wave approach is more oblique to the shoreline, increasing the alongshore redistribution of the sediment towards the SE, which may produce a sediment deficit on the NW part of the beach (up-wave). Moreover, the obliquity of the beach to the dominant westerly winds provides a long fetch distance, increasing aeolian transport down-drift and towards the dunes (Bauer et al., 2009).

6.1.4. Pays-de-Monts

The variable responses of the Pays-de-Monts site during the two periods are principally explained by the proximity of the Fromentine tidal inlet associated with the combination of wave and current processes that will not be discussed here (Bertin et al., 2013; Dodet et al., 2013; Hansen et al., 2013). At some distance from the tidal inlet, the beach responses seem to become more uniform showing minor alongshore variations (Fig. 11a, b) such as the beach response observed along the Gironde coast (Castelle et al., 2017) or like the complete foredune removal described in Priestas and Fagherazzi (2010). Mechanisms are dominated by rhythmic upper beach lowering and foredune retreat during period 1, and upper beach and foredune recovery during period 2 through the building of an embryo dune where space was left by erosion (Figs. 9c, 11b) (Thom and Hall, 1991; Suanez et al., 2012).

6.2. Probabilistic threshold efficiency and effect on sediment budgets

Geomorphic change detection using DEM differencing provides a comprehensive assessment of topographic evolution both qualitatively and quantitatively. Dealing with uncertainties remains a central issue when interpreting or establishing confidence in the results of a DoD (Wheaton et al., 2010; James et al., 2012) (James et al., 2012; Wheaton et al., 2010). A detection threshold is used to take account of the uncertainty in the analysis. As described in Section 1, it can be determined in three different ways, based on: (1) DEM comparison with more accurate ground control points, (2) comparison of flat hard surfaces between two DEMs, (3) the propagated uncertainty of each DEM given at a user-defined confidence interval (used in this paper). The visual interpretation of the DoD maps enables a qualitative assessment of the sensitivity of the results to a defined threshold, depending on the methodology. Without the availability of ground control points, methodologies (2) and (3) are compared with unthresholded results in Fig. 12. It can be seen that the detection threshold determined by methodology (2) is not high enough to exclude noise interferences that can influence the sediment budget (Table 3). A higher threshold is determined by methodology (3), which enables changes due to measurement errors to be better filtered. This may be considered too conservative (Table 3) because only significant changes that are 95% probable not due to error measurements remain in the analysis. Unfortunately, the raw datasets were not available for the study sites of this paper. Furthermore, in order to assess quantitatively the efficiency of a detection threshold, the results of a thresholded DoD should be compared with those of a DoD obtained with datasets surveyed at the same time but at higher accuracy and resolution. However, such datasets are rarely available.

On raw DoD maps the entire grid is represented, whereas on thresholded DoD maps the number of accounted grid cells is reduced. In fact, depending on the site and the period, between 8% and 25% of the area of thresholded DoD maps displays significant changes, while the rest is uncertain. Some large areas known to be stable, e.g. the back dune, are left intentionally in the grid in order to control the efficiency of the threshold. For this reason, study sites with large back dunes have a low percentage of significant changes (Table 4). On the contrary, the tidal beach, the upper beach and the foredune can display variable percentages of area showing significant changes of up to 71%, while the value for the back dune is never higher than 4%.

In terms of volume calculations, the raw net volume difference always overestimates the absolute value of sediment budgets considering the whole area at every site and period (Table 4). The back dune shows many non-significant changes over wide areas, which will heavily influence raw sediment budgets in either erosion or deposition. In some rarer cases, the net sediment budget is inverted from positive to negative or the reverse when the probabilistic threshold is applied (Table 4).

Geomorphic change detection using DEM differencing is better adapted to analyze and interpret geomorphic evolution with significant changes relative to the inherent uncertainty of the datasets (James et al., 2012). Although the probabilistic thresholding appears to exclude the best noise interference, it may be too conservative in some areas where changes are too small to be detected as significant (Fig. 12 and Table 3). For example, on a beach dominated by a cross-shore response, the sand eroded by a storm at the foredune is generally transported onto the tidal beach (Wright and Short, 1984; Short, 1991; Cooper et al., 2000). Changes at the foredune may appear as significant erosion, with change values above the detection threshold, while the sand deposited as an adjustment of the equilibrium beach profile on the tidal beach may cause small changes below the detection threshold, but spread out over a wide area. As Pye and Blott (2016) warned against the effect of errors between DEMs in volume difference calculations, small changes in elevation over large areas like the tidal beach can have a large impact on the total sediment budget. As an example in this paper, uniform dune undercutting causes significant erosion in

Fig. 10. Geomorphic change detection results for the Tresson site: (a) 2008–2010 DoD, (b) sediment buget segregation of the 2008–2010 period, (c) 2010–2013 DoD, (d) sediment budget segregation of the 2010–2013 period. This figure is available in colour online at https://www.journals.elsevier.com/geomorphology.

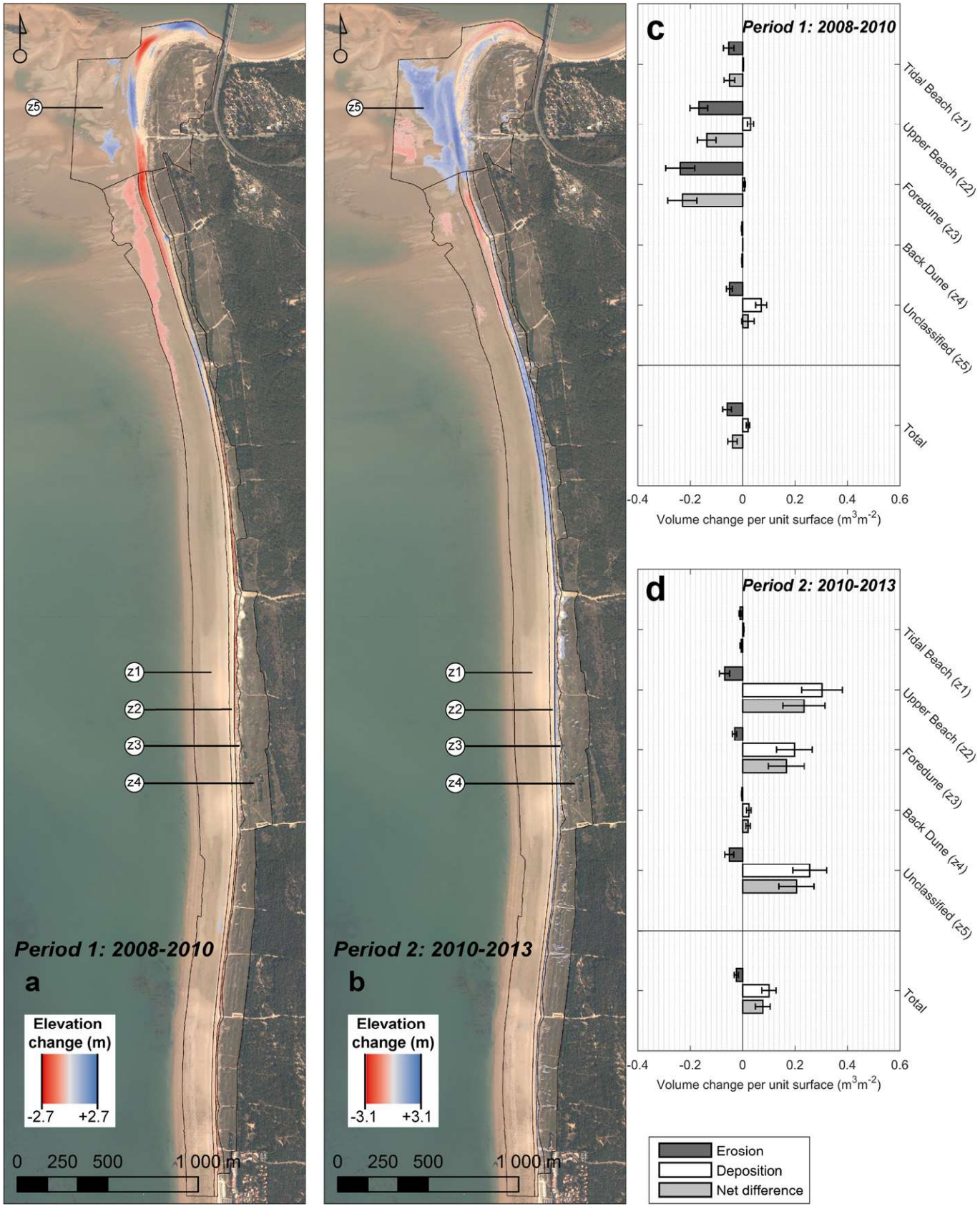

Fig. 11. Geomorphic change detection results for the Pays-de-Monts site: (a) 2008–2010 DoD, (b) 2010–2013 DoD, (c) sediment buget segregation of the 2008–2010 period, (d) sediment budget segregation of the 2010–2013 period. This figure is available in colour online at https://www.journals.elsevier.com/geomorphology.

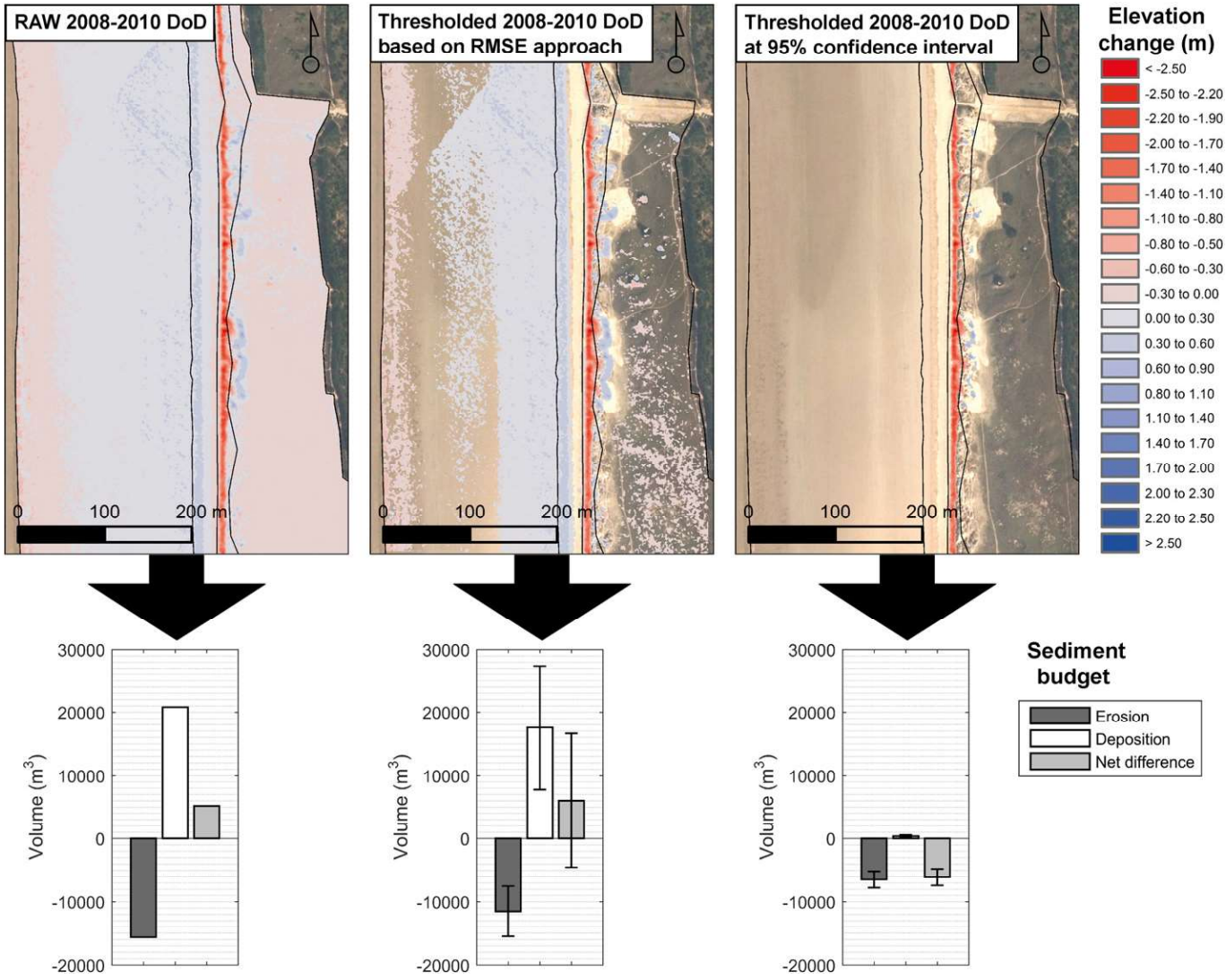

Fig. 12. Comparison between raw results, thresholded results with the RMSE approach, and thresholded results with the probalistic approach at a 95% confidence interval, on a small section of the Pays-de-Monts site using the 2008–2010 DoD. This figure is available in colour online at https://www.journals.elsevier.com/geomorphology.

the thresholded Pays-de-Monts DoD of the 2008–2010 period (Figs. 11, 12), while almost no significant change is detected on the tidal beach where we can expect deposition as an adjustment of the equilibrium beach profile. In DEM differencing, accounting for uncertainty through a reliable detection threshold can successfully filter small changes due to error measurements, but can also mask beach processes causing a small change in elevation over a wide area.

The recovery processes of a beach dune system starts right after the end of a storm and recovery mechanisms can be observed within days (Wang et al., 2006). These processes can also last until a new equilibrium is reached or a new storm event occurs (Woodroffe, 2007; Suanez et al., 2012; Houser et al., 2015). The 2008 and 2010 LiDAR datasets were surveyed 3 months and 6 months, respectively, after storms Johanna and Xynthia, which is why the impact of the storms may have been underestimated by comparing the two DEMs as the study sites may have already experienced some recovery. The recovery phase is analyzed by comparing two datasets collected at a three-year interval in the same season, i.e. the end of summer 2010 and the end of summer 2013. Even though period 2 was not exempt from winter storms - including Joachim in 2011, which certainly had a relative impact on the beach system three years after the last major storm tide - the three study sites seem to have fully recovered. Two reasons suggest this hypothesis: (i) the net sediment budget over the two periods is positive for the three study sites (Table 4), (ii) the seaward displacements of the dune base during period 2 reaches generally higher magnitudes than displacements in any direction during period 1 (Fig. 9) thanks to the building of embryo dunes (Figs. 8c, 10c, 11b).

Airborne LiDAR surveys are still expensive and sporadically collected. LiDAR data provide a "snapshot" of the beach state at the time of the survey (Woolard and Colby, 2002; Pye and Blott, 2016) which is strongly influenced by a combination of short-term and long-term processes interacting on the beach at different scales (Cowell and Thom, 1995). As the comparison of two datasets only provides the cumulative result of short-, medium-, and long-scale processes occurring on the beach, it can be very difficult to identify the contribution of an isolated event or a sequence of storms and the associated recovery in longer-scale beach evolution on a seasonal timescale or climate oscillation (Lee et al., 1998; Ranasinghe et al., 2004; Scott et al., 2016; Castelle et al., 2017). As an example, the interpretation of the beach evolution in this paper is complicated because of the temporal scale and the irregular frequency at which LiDAR surveys were carried out. To understand fully the changing morphology of a beach dune system from the event scale to long-term evolution, a "snapshot" of the beach elevation should be surveyed within a long-lasting or even permanent

project at least twice a year (Pye and Blott, 2016) or more frequently on a regular basis (Andrews et al., 2002; Woolard and Colby, 2002). The newly developed radar waterline method (Bell et al., 2016; Bird et al., 2017), which allows repeated surveys at high temporal resolution to quantify morphological change over large areas, seems to be a sound alternative or a support to low-frequency LiDAR campaigns.

7. Conclusion

1) The automatic extraction of geomorphic beach features from the DEMs, such as the dune base (D_{low}) and the dune crest (D_{high}), have a satisfactory success ratio despite differences in dune morphology between the three study sites. More difficulties were found in the 2013 DEM due to the smoother topographic break between the beach and the dune. Even though the procedure still needs a visual check, it is more objective and reproducible over large areas than manual digitizing or field surveys.
2) The probabilistic thresholding of DoDs at a 95% confidence interval and the associated volumetric calculations provide the most reliable results. However, caution should be taken when interpreting thresholded maps of changes and sediment budgets because some beach processes may be masked. No significant change in the thresholded DoD does not mean no change at all, but rather that the changes are not great enough, relative to the accuracy of the measurements, to be rigorously integrated in the results.
3) Site-specific geomorphological settings, particularly beach orientation and local sediment supply, are the main factors explaining the high variability of the beach responses between and within the three study sites. Due to the low temporal resolution and frequency of the LiDAR surveys used in this research, the attribution of the observed beach changes to storms events and the associated recovery can only be inferred with caution.
4) Despite site-specific mechanisms, recovery processes redistribute the available sand more on the upper parts of the beach, producing significant deposition generally in the form of embryo dunes. During the three years separating the 2010 and 2013 DEMs identified as the recovery phase, the beach and dune systems of the three study sites seem to have largely recovered.

Acknowledgments

The authors would like to thank Pays de la Loire region and three research programs (GERRICO, RS2E and the last one OR2C Regional Observatory of Coastal Risks of Pays-de-la-Loire region) for funding of LiDAR airborne campaigns, OSUNA for providing research facilities, the CEREMA for providing the wave measurements of the Yeu Buoy, and the SHOM for providing tide gauge observations. We also thank Carol Robins and Armelle Decaulne for proof-reading this paper. Finally, we are grateful for the careful review by anonymous reviewers and editor whose constructive feedback really improved this manuscript.

Appendix A. Supplementary data

Supplementary data associated with this article can be found in the online version, at https://doi.org/10.1016/j.geomorph.2017.12.037. These data includes the Google map of the most important areas described in this article.

References

Andrews, B., Gares, P.A., Colby, J.D., 2002. Techniques for GIS modeling of coastal dunes. Geomorphology. 29th Binghamton Geomorphology Symposium: Coastal Geomorphology vol. 48:pp. 289–308. https://doi.org/10.1016/S0169-555X(02)00186-1.

Autret, R., Dodet, G., Fichaut, B., Suanez, S., David, L., Leckler, F., Ardhuin, F., Ammann, J., Grandjean, P., Allemand, P., Filipot, J.-F., 2016. A comprehensive hydro-geomorphic study of cliff-top storm deposits on Banneg Island during winter 2013–2014. Mar. Geol. 382:37–55. https://doi.org/10.1016/j.margeo.2016.09.014.

Ba, A., Patrick, L., Robin, M., Moussaoui, S., Cyril, M., Giraud, M., Le Menn, E., 2015. Apport du LiDAR dans le géoréférencement d'images hyperspectrales en vue d'un couplage LiDAR/hyperspectral. Rev. Fr. Photogrammétrie Télédétection 5–15.

Baptista, P., Bastos, L., Bernardes, C., Cunha, T., Dias, J., 2008. Monitoring sandy shores morphologies by DGPS: a practical tool to generate digital elevation models. J. Coast. Res. 24 (6), 1516–1528.

Bauer, B.O., Davidson-Arnott, R.G.D., Hesp, P.A., Namikas, S.L., Ollerhead, J., Walker, I.J., 2009. Aeolian sediment transport on a beach: surface moisture, wind fetch, and mean transport. Geomorphology. Contemporary Research in Aeolian Geomorphology 6th International Conference on Aeolian Research (ICAR VI) vol. 105:pp. 106–116. https://doi.org/10.1016/j.geomorph.2008.02.016.

Bell, P.S., Bird, C.O., Plater, A.J., 2016. A temporal waterline approach to mapping intertidal areas using X-band marine radar. Coast. Eng. 107:84–101. https://doi.org/10.1016/j.coastaleng.2015.09.009.

Bertin, X., Castelle, B., Anfuso, G., Ferreira, Ó., 2007. Improvement of sand activation depth prediction under conditions of oblique wave breaking. Geo-Mar. Lett. 28:65–75. https://doi.org/10.1007/s00367-007-0090-2.

Bertin, X., Bruneau, N., Breilh, J.-F., Fortunato, A.B., Karpytchev, M., 2012. Importance of wave age and resonance in storm surges: the case Xynthia, Bay of Biscay. Ocean Model 42:16–30. https://doi.org/10.1016/j.ocemod.2011.11.001.

Bertin, X., Dodet, G., Fortunato, A., Bruneau, N., 2013. A review of the processes controlling the dynamics of wave-dominated inlets. Coastal Dynamics 2013. Presented at the Coastal Dynamics 2013, Arcachon, pp. 173–182.

Bertin, X., Li, K., Roland, A., Zhang, Y.J., Breilh, J.F., Chaumillon, E., 2014. A modeling-based analysis of the flooding associated with Xynthia, central Bay of Biscay. Coast. Eng. 94: 80–89. https://doi.org/10.1016/j.coastaleng.2014.08.013.

Bertin, X., Li, K., Roland, A., Bidlot, J.-R., 2015. The contribution of short-waves in storm surges: two case studies in the Bay of Biscay. Cont. Shelf Res. 96:1–15. https://doi.org/10.1016/j.csr.2015.01.005.

Bird, C.O., Bell, P.S., Plater, A.J., 2017. Application of marine radar to monitoring seasonal and event-based changes in intertidal morphology. Geomorphology 285:1–15. https://doi.org/10.1016/j.geomorph.2017.02.002.

Boak, E.H., Turner, I.L., 2005. Shoreline definition and detection: a review. J. Coast. Res. 21 (4):688–703. https://doi.org/10.2112/03-0071.1.

Brasington, J., Rumsby, B.T., McVey, R.A., 2000. Monitoring and modelling morphological change in a braided gravel-bed river using high resolution GPS-based survey. Earth Surf. Process. Landf. 25:973–990. https://doi.org/10.1002/1096-9837(200008)25:9<973::AID-ESP111>3.0.CO;2-Y.

Brasington, J., Langham, J., Rumsby, B., 2003. Methodological sensitivity of morphometric estimates of coarse fluvial sediment transport. Geomorphology 53:299–316. https://doi.org/10.1016/S0169-555X(02)00320-3.

Brock, J.C., Purkis, S.J., 2009. The emerging role of lidar remote sensing in coastal research and resource management. J. Coast. Res. 53:1–5. https://doi.org/10.2112/SI53-001.1.

Brock, J.C., Krabill, W., Sallenger, A.H., 2004. Barrier island morphodynamic classification based on lidar metrics for North Assateague Island, Maryland. J. Coast. Res. 20 (2), 498–509.

Brunsden, D., 2001. A critical assessment of the sensitivity concept in geomorphology. Catena. Landscape Sensitivity: Principles and Applications in Northern 42:pp. 99–123. https://doi.org/10.1016/S0341-8162(00)00134-X.

Burvingt, O., Masselink, G., Russell, P., Scott, T., 2017. Classification of beach response to extreme storms. Geomorphology 295:722–737. https://doi.org/10.1016/j.geomorph.2017.07.022.

Butel, R., Dupuis, H., Bonneton, P., 2002. Spatial variability of wave conditions on the French Atlantic coast using in-situ data. J. Coast. Res. 36, 96–108.

Castelle, B., Bujan, S., Ferreira, S., Dodet, G., 2017. Foredune morphological changes and beach recovery from the extreme 2013/2014 winter at a high-energy sandy coast. Mar. Geol. 385:41–55. https://doi.org/10.1016/j.margeo.2016.12.006.

Chaumillon, E., Proust, J.-N., Menier, D., Weber, N., 2008. Incised-valley morphologies and sedimentary-fills within the inner shelf of the northern Bay of Biscay. J. Mar. Syst. 72: 383–396. https://doi.org/10.1016/j.jmarsys.2007.05.014.

Coco, G., Senechal, N., Rejas, A., Bryan, K.R., Capo, S., Parisot, J.P., Brown, J.A., MacMahan, J.H.M., 2014. Beach response to a sequence of extreme storms. Geomorphology 204:493–501. https://doi.org/10.1016/j.geomorph.2013.08.028.

Cook, K.L., 2017. An evaluation of the effectiveness of low-cost UAVs and structure from motion for geomorphic change detection. Geomorphology 278:195–208. https://doi.org/10.1016/j.geomorph.2016.11.009.

Cooper, N.J., Leggett, D.J., Lowe, J.P., 2000. Beach-profile measurement, theory and analysis: practical guidance and applied case studies. Water Environ. J. 14:79–88. https://doi.org/10.1111/j.1747-6593.2000.tb00231.x.

Cooper, J.A.G., Jackson, D.W.T., Navas, F., McKenna, J., Malvarez, G., 2004. Identifying storm impacts on an embayed, high-energy coastline: examples from western Ireland. Mar. Geol. 210:261–280. https://doi.org/10.1016/j.margeo.2004.05.012.

Cowell, P.J., Thom, B.G., 1995. Morphodynamics of coastal evolution. Coastal Evolution. Cambridge University Press.

Crapoulet, A., Héquette, A., Marin, D., Levoy, F., Bretel, P., 2017. Variations in the response of the dune coast of northern France to major storms as a function of available beach sediment volume. Earth Surf. Process. Landf. https://doi.org/10.1002/esp.4098 (n/a-n/a).

Creach, A., Pardo, S., Guillotreau, P., Mercier, D., 2015. The use of a micro-scale index to identify potential death risk areas due to coastal flood surges: lessons from Storm Xynthia on the French Atlantic coast. Nat. Hazards 77:1679–1710. https://doi.org/10.1007/s11069-015-1669-y.

CREOCEAN, 2011. Etude du Fonctionnement Hydro-sédimentaire et Solutions de Stabilisation du chenal de Fromentine - Rapport de la Phase 2: Analyse du Fonctionnement Hydro-sédimentaire du système. Conseil Général de Vendée ((No. 1–10253–I). La Rochelle).

Crowell, M., Leatherman, S.P., Buckley, M.K., 1991. Historical shoreline change: error analysis and mapping accuracy. J. Coast. Res. 7 (3), 839–852.
Davies, J.L., 1964. A morphogenetic approach to world shorelines. Z. Geomorphol. 8, 127–142.
Davis, R.A., FitzGerald, D.M., 2004. Beaches and Coasts. Nachdr. ed. Blackwell Publ, Malden, Mass.
Dean, R.G., 1991. Equilibrium beach profiles: characteristics and applications. J. Coast. Res. 7.
DHI, GEOS, 2008. Étude de Connaissance Des phénomènes d'érosion sur le Littoral Vendéen – DDTM85 (Final Report), Nantes.
Dodet, G., Bertin, X., Taborda, R., 2010. Wave climate variability in the North-East Atlantic Ocean over the last six decades. Ocean Model 31:120–131. https://doi.org/10.1016/j.ocemod.2009.10.010.
Dodet, G., Bertin, X., Bruneau, N., Fortunato, A.B., Nahon, A., Roland, A., 2013. Wave-current interactions in a wave-dominated tidal inlet. J. Geophys. Res. Oceans 118: 1587–1605. https://doi.org/10.1002/jgrc.20146.
Dolan, R., Davis, R.E., 1992. An intensity scale for Atlantic Coast northeast storms. J. Coast. Res. 8, 840–853.
Dolan, R., Fenster, M.S., Holme, S.J., 1991. Temporal analysis of shoreline recession and accretion. J. Coast. Res. 7, 723–744.
Elko, N., Guy, K., Stockdon, H., Morgan, K., 2002. Barrier island elevations relevant to potential storm impacts: 1. Techniques (No. USGS Open File Report 02-287).
Esteves, L.S., Brown, J.M., Williams, J.J., Lymbery, G., 2012. Quantifying thresholds for significant dune erosion along the Sefton Coast, Northwest England. Geomorphology. Thresholds for Storm Impacts Along European Coastlines 143–144:pp. 52–61. https://doi.org/10.1016/j.geomorph.2011.02.029.
Evans, O.F., 1942. The origin of spits, bars, and related structures. J. Geol. 50:846–865. https://doi.org/10.1086/625087.
Fattal, P., Robin, M., Paillart, M., Maanan, M., Mercier, D., Lamberts, C., Costa, S., 2010. Effets des tempêtes sur une plage aménagée et à forte protection côtière: la plage des Éloux (côte de Noirmoutier, Vendée, France). Norois no. 215. pp. 101–114.
Gao, Y., 2009. Algorithms and Software Tools for Extracting Coastal Morphological Information From Airborne LiDAR Data. MSc thesis. A&M University, Texas.
Hansen, J.E., Elias, E., Barnard, P.L., 2013. Changes in surfzone morphodynamics driven by multi-decadal contraction of a large ebb-tidal delta. Mar. Geol. A Multi-discipline Approach for Understanding Sediment Transport and Geomorphic Evolution in an Estuarine-coastal System: San Francisco Bay 345:pp. 221–234. https://doi.org/10.1016/j.margeo.2013.07.005
Hardin, E., Kurum, M.O., Mitasova, H., Overton, M.F., 2012. Least cost path extraction of topographic features for storm impact scale mapping. J. Coast. Res. 28 (4):970–978. https://doi.org/10.2112/JCOASTRES-D-11-00126.1.
Harley, M.D., Turner, I.L., Short, A.D., 2015. New insights into embayed beach rotation: The importance of wave exposure and cross-shore processes. J. Geophys. Res. Earth Surf. 120, 2014JF003390. https://doi.org/10.1002/2014JF003390.
Hayes, M.O., 1980. General morphology and sediment patterns in tidal inlets. Sediment. Geol. 26:139–156. https://doi.org/10.1016/0037-0738(80)90009-3.
Héquette, A., Ruz, M.-H., 1991. Spit and barrier island migration in the southeastern Canadian Beaufort Sea. J. Coast. Res. 7, 677–698.
Hesp, P., 2002. Foredunes and blowouts: initiation, geomorphology and dynamics. Geomorphology. 29th Binghamton Geomorphology Symposium: Coastal Geomorphology 48:pp. 245–268. https://doi.org/10.1016/S0169-555X(02)00184-8.
Houser, C., Hamilton, S., 2009. Sensitivity of post-hurricane beach and dune recovery to event frequency. Earth Surf. Process. Landf. 34:613–628. https://doi.org/10.1002/esp.1730.
Houser, C., Hapke, C., Hamilton, S., 2008. Controls on coastal dune morphology, shoreline erosion and barrier island response to extreme storms. Geomorphology 100: 223–240. https://doi.org/10.1016/j.geomorph.2007.12.007.
Houser, C., Wernette, P., Rentschlar, E., Jones, H., Hammond, B., Trimble, S., 2015. Post-storm beach and dune recovery: implications for barrier island resilience. Geomorphology 234:54–63. https://doi.org/10.1016/j.geomorph.2014.12.044.
Hugenholtz, C.H., Barchyn, T.E., 2010. Spatial analysis of sand dunes with a new global topographic dataset: new approaches and opportunities. Earth Surf. Process. Landf. 35: 986–992. https://doi.org/10.1002/esp.2013.
Hugenholtz, C.H., Levin, N., Barchyn, T.E., Baddock, M.C., 2012. Remote sensing and spatial analysis of aeolian sand dunes: a review and outlook. Earth-Sci. Rev. 111:319–334. https://doi.org/10.1016/j.earscirev.2011.11.006.
James, L.A., Hodgson, M.E., Ghoshal, S., Latiolais, M.M., 2012. Geomorphic change detection using historic maps and DEM differencing: the temporal dimension of geospatial analysis. Geomorphology. Geospatial Technologies and Geomorphological Mapping Proceedings of the 41st Annual Binghamton Geomorphology Symposium 137: pp. 181–198. https://doi.org/10.1016/j.geomorph.2010.10.039.
Krabill, W.B., Wright, C.W., Swift, R.N., Frederick, E.B., Manizade, S.S., Yungel, J.K., Martin, C.F., Sonntag, J.G., Duffy, M., Hulslander, W., Brock, J.C., 2000. Airborne laser mapping of Assateague National Seashore Beach. Photogramm. Eng. Remote. Sens. 66, 6571.
Lee, G., Nicholls, R.J., Birkemeier, W.A., 1998. Storm-driven variability of the beach-nearshore profile at Duck, North Carolina, USA, 1981–1991. Mar. Geol. 148:163–177. https://doi.org/10.1016/S0025-3227(98)00010-3.
Liu, X., Zhang, Z., 2008. LiDAR data reduction for efficient and high quality DEM generation. Int. Arch. Photogramm. Remote. Sens. Spat. Inf. Sci. 37, 173–178.
Mancini, F., Dubbini, M., Gattelli, M., Stecchi, F., Fabbri, S., Gabbianelli, G., 2013. Using unmanned aerial vehicles (UAV) for high-resolution reconstruction of topography: the structure from motion approach on coastal environments. Remote Sens. 5: 6880–6898. https://doi.org/10.3390/rs5126880.
Masselink, G., Scott, T., Poate, T., Russell, P., Davidson, M., Conley, D., 2016. The extreme 2013/2014 winter storms: hydrodynamic forcing and coastal response along the southwest coast of England. Earth Surf. Process. Landf. 41:378–391. https://doi.org/10.1002/esp.3836.
Mitasova, H., Hardin, E., Starek, M.J., Harmon, R.S., Overton, M., 2011. Landscape dynamics from LiDAR data time series. In: Hengl, T., Evans, I.S., Wilson, J.P., Gould, M. (Eds.), Geomorphometry. Redlands, California, pp. 3–6. http://geomorphometry.org/Mitasova.
Moore, L.J., 2000. Shoreline mapping techniques. J. Coast. Res. 16, 111–124.
Moore, L.J., Ruggiero, P., List, J.H., 2006. Comparing mean high water and high water line shorelines: should prosy-datum offsets be incorporated into shoreline change analysis? J. Coast. Res. 22:12. https://doi.org/10.2112/04-0401.1.
Morzadec-Kerfourn, M.-T., 1995. Coastline changes in the Armorican Massif (France) during the Holocene. J. Coast. Res. 197–203.
Palaseanu-Lovejoy, M., Danielson, J., Thatcher, C., Foxgrover, A., Barnard, P., Brock, J., Young, A., 2016. Automatic delineation of seacliff limits using lidar-derived high-resolution DEMs in Southern California. J. Coast. Res.:162–173. https://doi.org/10.2112/SI76-014.
Pastol, Y., 2011. Use of airborne LIDAR bathymetry for coastal hydrographic surveying: the French experience. J. Coast. Res. 62:6–18. https://doi.org/10.2112/SI_62_2.
Pineau-Guillou, L., Lathuiliere, C., Magne, R., Louazel, S., Corman, D., Perherin, C., 2012. Sea levels analysis and surge modelling during storm Xynthia. Eur. J. Environ. Civ. Eng. 16:943–952. https://doi.org/10.1080/19648189.2012.676424.
Priestas, A.M., Fagherazzi, S., 2010. Morphological barrier island changes and recovery of dunes after Hurricane Dennis, St. George Island, Florida. Geomorphology 114: 614–626. https://doi.org/10.1016/j.geomorph.2009.09.022.
Pye, K., Blott, S.J., 2008. Decadal-scale variation in dune erosion and accretion rates: an investigation of the significance of changing storm tide frequency and magnitude on the Sefton coast, UK. Geomorphology 102:652–666. https://doi.org/10.1016/j.geomorph.2008.06.011.
Pye, K., Blott, S.J., 2016. Assessment of beach and dune erosion and accretion using LiDAR: impact of the stormy 2013–14 winter and longer term trends on the Sefton Coast, UK. Geomorphology 266:146–167. https://doi.org/10.1016/j.geomorph.2016.05.011.
Ranasinghe, R., McLoughlin, R., Short, A., Symonds, G., 2004. The Southern Oscillation Index, wave climate, and beach rotation. Mar. Geol. 204:273–287. https://doi.org/10.1016/S0025-3227(04)00002-7.
Rivière, G., Arbogast, P., Lapeyre, G., Maynard, K., 2012. A potential vorticity perspective on the motion of a mid-latitude winter storm. Geophys. Res. Lett. 39, L12808. https://doi.org/10.1029/2012GL052440.
Robertson, W., Zhang, K., Whitman, D., 2007. Hurricane-induced beach change derived from airborne laser measurements near Panama City, Florida. Mar. Geol. 237: 191–205. https://doi.org/10.1016/j.margeo.2006.11.003.
Ruggerio, P., Kratzmann, M.G., Himmelstoss, E.A., Reid, D., Allan, J., Kaminsky, G., 2013. National assessment of shoreline change: historical shoreline change along the Pacific Northwest coast (Report No. 2012–1007). Open-File Report. Reston, VA. https://doi.org/10.3133/ofr20121007.
Ruggiero, P., Kaminsky, G.M., Gelfenbaum, G., 2003. Linking proxy-based and datum-based shorelines on a high-energy coastline: implications for shoreline change analyses. J. Coast. Res. 38, 57–82.
Rutzinger, M., Höfle, B., Kringer, K., 2012. Accuracy of automatically extracted geomorphological breaklines from airborne LiDAR curvature images. Geogr. Ann. Ser. Phys. Geogr. 94:33–42. https://doi.org/10.1111/j.1468-0459.2012.00453.x.
Ruz, M.-H., Meur-Ferec, C., 2004. Influence of high water levels on aeolian sand transport: upper beach/dune evolution on a macrotidal coast, Wissant Bay, northern France. Geomorphology 60:73–87. https://doi.org/10.1016/j.geomorph.2003.07.011.
Sallenger Jr., A.H., Krabill, W.B., Swift, R.N., Brock, J., List, J., Hansen, M., Holman, R.A., Manizade, S., Sontag, J., Meredith, A., Morgan, K., Yunkel, J.K., Frederick, E.B., Stockdon, H., 2003. Evaluation of airborne topographic lidar for quantifying beach changes. J. Coast. Res. 19 (1), 125–133.
Saye, S.E., van der Wal, D., Pye, K., Blott, S.J., 2005. Beach–dune morphological relationships and erosion/accretion: an investigation at five sites in England and Wales using LIDAR data. Geomorphology 72:128–155. https://doi.org/10.1016/j.geomorph.2005.05.007.
Scott, T., Masselink, G., O'Hare, T., Saulter, A., Poate, T., Russell, P., Davidson, M., Conley, D., 2016. The extreme 2013/2014 winter storms: beach recovery along the southwest coast of England. Mar. Geol. https://doi.org/10.1016/j.margeo.2016.10.011.
SHOM, 2014. Références Altimétriques Maritimes (RAM). Ports de France Métropolitaine et d'outre-mer. Cotes du zéro Hydrographique et Niveaux Caractéristiques de la Marée. Service Hydrographique et Océanographique de la Marine, Brest.
Short, A.D., 1991. Macro-meso tidal beach morphodynamics: an overview. J. Coast. Res. 7 (2), 417–436.
Stockdon, H.F., Asbury, H., Sallenger, J., List, J.H., Holman, R.A., 2002. Estimation of shoreline position and change using airborne topographic lidar data. J. Coast. Res. 18 (3), 502–513.
Stockdon, H.F., Doran, K.S., Sallenger, A.H., 2009. Extraction of lidar-based dune-crest elevations for use in examining the vulnerability of beaches to inundation during hurricanes. J. Coast. Res. 53:59–65. https://doi.org/10.2112/SI53-007.1.
Suanez, S., Cariolet, J.-M., Cancouët, R., Ardhuin, F., Delacourt, C., 2012. Dune recovery after storm erosion on a high-energy beach: Vougot Beach, Brittany (France). Geomorphology 139–140:16–33. https://doi.org/10.1016/j.geomorph.2011.10.014.
Taylor, J.R., 1997. An Introduction to Error Analysis: The Study of Uncertainties in Physical Measurements. 2nd ed. University Science Books, Sausalito, Calif.
Ters, M., 1961. La Vendee Littorale: Étude de Géomorphologie. Rennes, Paris.
Thom, B.G., Hall, W., 1991. Behaviour of beach profiles during accretion and erosion dominated periods. Earth Surf. Process. Landf. 16:113–127. https://doi.org/10.1002/esp.3290160203.
Thomas, T., Phillips, M.R., Williams, A.T., Jenkins, R.E., 2012. Rotation on two adjacent open coast macrotidal beaches. Appl. Geogr. 35:363–376. https://doi.org/10.1016/j.apgeog.2012.08.010.

Thornton, E.B., Sallenger, A., Sesto, J.C., Egley, L., McGee, T., Parsons, R., 2006. Sand mining impacts on long-term dune erosion in southern Monterey Bay. Mar. Geol. 229:45–58. https://doi.org/10.1016/j.margeo.2006.02.005.

Tolman, H.L., 2009. User Manual and System Documentation of WAVEWATCH III TM version 3.14.

Turki, I., Medina, R., Coco, G., Gonzalez, M., 2013. An equilibrium model to predict shoreline rotation of pocket beaches. Mar. Geol. 346:220–232. https://doi.org/10.1016/j.margeo.2013.08.002.

Verger, F., 2009. Zones Humides du Littoral Français: Estuaires, Deltas, Marais et Lagunes. Belin, Paris.

Wang, P., Kirby, J.H., Haber, J.D., Horwitz, M.H., Knorr, P.O., Krock, J.R., 2006. Morphological and sedimentological impacts of Hurricane Ivan and immediate poststorm beach recovery along the northwestern Florida barrier-island coasts. J. Coast. Res. 22 (6): 1382–1402. https://doi.org/10.2112/05-0440.1.

Wheaton, J.M., 2008. Uncertainty in Morphological Sediment Budgeting of Rivers. PhD thesis. University of Southampton.

Wheaton, J.M., Brasington, J., Darby, S.E., Sear, D.A., 2010. Accounting for uncertainty in DEMs from repeat topographic surveys: improved sediment budgets. Earth Surf. Process. Landf. 35:136–156. https://doi.org/10.1002/esp.1886.

White, S.A., Wang, Y., 2003. Utilizing DEMs derived from LIDAR data to analyze morphologic change in the North Carolina coastline. Remote Sens. Environ. 85: 39–47. https://doi.org/10.1016/S0034-4257(02)00185-2.

White, S.A., Parrish, C.E., Calder, B.R., Pe'eri, S., Rzhanov, Y., 2011. LIDAR-derived national shoreline: empirical and stochastic uncertainty analyses. J. Coast. Res. 62:62–74. https://doi.org/10.2112/SI_62_7.

Witkin, A., 1984. Scale-space filtering: a new approach to multi-scale description. Acoustics, Speech, and Signal Processing. IEEE International Conference on ICASSP'84. IEEE, pp. 150–153.

Woodroffe, C., 2007. The natural resilience of coastal systems: primary concepts. In: McFadden, L., Penning-Rowsell, E., Nicholls, R.J. (Eds.), Managing Coastal Vulnerability. Elsevier, Amsterdam, pp. 45–60.

Woolard, J.W., Colby, J.D., 2002. Spatial characterization, resolution, and volumetric change of coastal dunes using airborne LIDAR: Cape Hatteras, North Carolina. Geomorphology. 29th Binghamton Geomorphology Symposium: Coastal Geomorphology 48:pp. 269–287. https://doi.org/10.1016/S0169-555X(02)00185-X.

Wright, L.D., Short, A.D., 1984. Morphodynamic variability of surf zones and beaches: a synthesis. Mar. Geol. 56:93–118. https://doi.org/10.1016/0025-3227(84)90008-2.

Young, A.P., Ashford, S.A., 2006. Application of airborne LIDAR for seacliff volumetric change and beach-sediment budget contributions. J. Coast. Res. 22 (2):307–318. https://doi.org/10.2112/05-0548.1.

Zhang, K., Douglas, B.C., Leatherman, S.P., 2001. Beach erosion potential for severe Nor'easters. J. Coast. Res. 17 (2), 309–321.

Zhang, K., Whitman, D., Leatherman, S., Robertson, W., 2005. Quantification of beach changes caused by hurricane Floyd along Florida's Atlantic Coast using airborne laser surveys. J. Coast. Res. 21 (1):123–134. https://doi.org/10.2112/02057.1.